

Single-Step Parity Check Gate Set for Quantum Error Correction

Gözde Üstün¹, Andrea Morello¹ and Simon Devitt²

¹ Centre for Quantum Computation and Communication Technology, School of Electrical Engineering and Telecommunications, University of New South Wales, Sydney, New South Wales 2052, Australia

² Centre for Quantum Software and Information University of Technology Sydney, Sydney, Australia

E-mail: g.ustun@unsw.edu.au

Abstract. A key requirement for an effective Quantum Error Correction (QEC) scheme is that the physical qubits have error rates below a certain threshold. The value of this threshold depends on the details of the specific QEC scheme, and its hardware-level implementation. This is especially important with parity-check circuits, which are the fundamental building blocks of QEC codes. The standard way of constructing the parity check circuit is using a universal set of gates, namely sequential CNOT gates, single-qubit rotations and measurements. We exploit the insight that a QEC code does not require universal logic gates, but can be simplified to perform the sole task of error detection and correction. By building gates that are fundamental to QEC, we can boost the threshold and ease the experimental demands on the physical hardware. We present a rigorous formalism for constructing and verifying the error behavior of these gates, linking the physical measurement of a process matrix to the abstract error models commonly used in QEC analysis. This allows experimentalists to directly map the gates used in their systems to thresholds derived for a broad-class of QEC codes. We give an example of these new constructions using the model system of two nuclear spins, coupled to an electron spin, showing the potential benefits of redesigning fundamental gate sets using QEC primitives, rather than traditional gate sets reliant on simple single and two-qubit gates.

Keywords: quantum error correction, fault-tolerant quantum computation, quantum control

1. Introduction

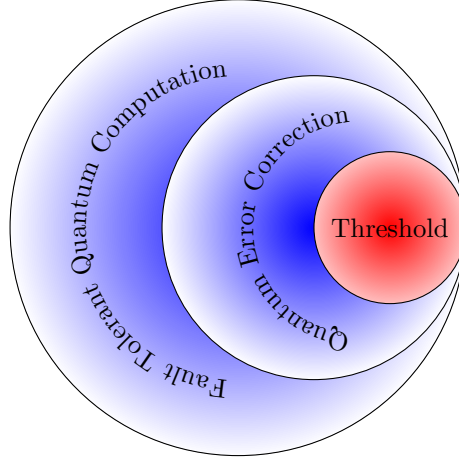


Figure 1: Hierarchy for scalability. The threshold is the core part for practical quantum error correction (QEC). The threshold is a fundamental and indispensable component in the realm of QEC. It serves as a critical benchmark for determining the efficacy of QEC schemes in correcting errors that occur in quantum systems. Without achieving a sufficiently high threshold, the practical implementation of QEC is rendered impractical, if not impossible. However, crossing the threshold is the point at which QEC becomes effective in correcting more errors than we introduce. The implementation of QEC can enable Fault Tolerant Quantum Computation (FTQC), which is crucial for realizing practical quantum applications that require high accuracy and reliability, such as Shor’s algorithm or quantum simulation. Therefore, achieving a high threshold not only ensures the feasibility of QEC, but also unlocks the potential for Fault Tolerant Quantum Computation (FTQC).

Being able to scale quantum computers is a necessary condition for useful quantum algorithms [1]. Algorithms with proven speed up, such as Shor’s factorization algorithm [2], quantum simulation [3] or the quantum algorithm for solving linear systems of equations (also known as the HHL (Harrow, Hassidim, Lloyd) algorithm [4]) only become useful when implemented on thousands of near-perfect qubits. As it is unlikely that physical error rates will be vanishingly small in the near term, the addition of Quantum Error Correction (QEC) and fault-tolerance is required. For practical QEC, the threshold value is the critical metric. This value is the point at which the error rate of physical qubits falls below a certain threshold, and any further reduction in error rate will result in the suppression of logical qubit errors to zero. This is the point where QEC becomes effective and corrects more

errors than we introduce. Conversely, if the error rate of physical qubits exceeds this threshold, the logical qubit errors will go to infinity. Therefore, the threshold value is the highest acceptable value of physical error per gate for each qubit, and this value should be as high as possible in order to ensure the efficacy of QEC [5][6] (Figure 1). The target of any quantum hardware is to attain the lowest possible errors, such that they fall below the necessary error threshold [7]. The value of this error threshold depends on the structure of the QEC scheme along with any subsequent fault-tolerant circuit and hardware implementations [8].

The surface code is a good example of a well-performing code that is, in principle, experimentally realizable [9][10][11][12]. It has a comparably high threshold which is highly dependent on the assumed underlying noise model. A noise model is an assumption which underlies the physics that dictates how noise manifests in a quantum system and it could include the pathological error channels such as qubit loss and leakage. By making these assumptions about how error syndromes are measured in the system, commonly referred to by terms such as code capacity, phenomenological models and circuit-based model [13], wildly different numbers can be obtained for the fault-tolerant threshold. The surface code requires the extraction of syndromes based on the parity of four-body operators, and these different noise models consider different ways in which the parity of these operators could be measured.

The code capacity and the phenomenological noise models are based on having natural four-body measurement. On the other hand, the circuit-based model constructs four-body parity check measurements by utilizing one-body Pauli (single qubit) measurements and standard quantum gates. This approach results in the lowest threshold for the code due to the accumulation of physical errors on these standard quantum gates throughout the circuit. The circuit-based noise model is the most experimentally precise analysis of the surface code, as effectively all experimental qubit systems do not have access to direct four-body measurements.

In this study, instead of trying to improve thresholds with the current sources, one body Pauli measurements, which are intrinsically built for universal computation, we redesign the universal gates, such that these gates become the most natural gate for QEC implementation. By building gates fundamental to QEC rather than universal computation, we can boost the threshold and ease the experimental difficulty to achieve the scalability. We believe that this modification to universal gate set is necessary because any large scale quantum computer will, by necessity,

be a QEC machine.

As primitives, the universality of error-correcting quantum computing requires only occasional use of gates which are traditionally associated with universal computation. However, QEC does require the definition of a new gate set, which is constructed by modifying the pre-existing universal gate set. Then, the question is how does an experimental system verify that the new gate set is implementable in the lab in a way that the implementation of the new gate set will allow us to increase the threshold of QEC.

In this work, we present a rigorous formalism for constructing and verifying a native gate set, which we denote as the single-step parity check (SSPC) gate set, designed specifically for QEC circuits. We then apply this technique to the two-body parity check circuits necessary for implementing the Honeycomb code [14]. We present the single-step parity check gates in the context of spin qubits [15], as we believe they are well-suited to realising more efficient, direct two-body measurements. However, this formalism applies more broadly and could be used for hardware systems that can naturally implement high dimensional parity check gate primitives.

This paper provides a comprehensive review of various concepts, with the aim of benefiting experimentalists. The organization of this paper is as follows: Section 2 briefly reviews the concept of multi-qubit measurements. In Section 3, noise models are explained in the context of the large history of work studying the surface code. In Section 4, the Honeycomb code is explained. In Section 5, current implementable noise model is defined and in Section 5.2 the drawback of this noise model is shown numerically by analyzing the experimental data [16]. In Section 6, The Single-step parity check gate set is explained and in Section 6.1, two-body parity check circuits which are constructed both using the universal gate set and the single-step parity check gate are compared in the presence of noise. In Section 6.2, we provide an example system of silicon spin qubits to implement the SSPC gate set. In section 7, we summarise the paper.

2. The Concept of Making Multi Qubit Parity Check Measurement

A qubit is a two level system and when we measure one qubit, we can have either 1 or 0 as a result. One corresponds odd parity and zero corresponds even parity. This is what a parity check is. Since we measure over one qubit, we are making a one-body parity measurement which is called M_{pp1} . Here pp refers to Pauli Product and

M_{pp1} refers to measuring in one Pauli basis, for example measuring in the Z basis. This is also what we implement in the lab today. All measurements are actually a parity check. When we measure a qubit in the computational basis in the lab, we actually measure the parity of the qubit. This can be generalized beyond a single qubit and it is useful in QEC. The idea of parity checks in QEC is to have just parity information of multiple data qubits over one (ancilla) qubit without revealing any other information. In other words, we are constructing $M_{ppi}, i = 2, 3, 4, \dots$ from M_{pp1} . For constructing M_{ppi} from M_{pp1} for a valid quantum observable U , we need to apply the controlled-U gates between the ancilla qubit and the data qubits sequentially. For example, for making parity check measurement in the X basis, we need to apply CNOT gates between the ancilla qubit and the data qubits sequentially since the controlled gate in this case is a CNOT (CX) gate.

Although any unitary can be used for the parity check, we are going to give an example over the well known parity check measurements in QEC. For example, if we have an XX , where $XX = X \otimes X$, parity check measurement, we will have two CNOT gates or if we want to have an $XXXX$, where $XXXX = X \otimes X \otimes X \otimes X$, parity check measurement, we will have four CNOT gates and since we measure the system over one (ancilla) qubit, we use M_{pp1} . ‡

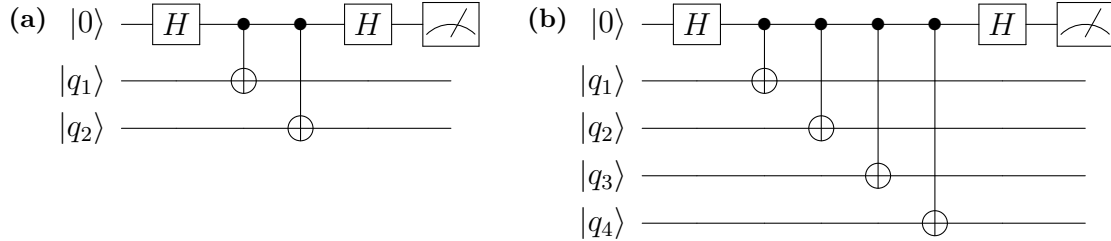


Figure 2: XX and $XXXX$ parity check measurements using M_{pp1} . a) a two-body parity check circuit. This circuit allows us to learn the parity information of the two qubits in the X basis by applying CNOT gates between the ancilla and q_1 and q_2 sequentially and then measuring the ancilla - M_{pp1} -. b) a four-body parity check circuit. This circuit allows us to learn the parity information of four qubits in the X basis by applying CNOT gates between the ancilla and four qubits sequentially and then measuring the ancilla - M_{pp1} -.

Let us look at Figure 2a closer to understand what a parity check does to a state.

‡ Any valid quantum observable can be used for the parity check, this is determined by the operator on the target side of the controlled gate. In Figure 2a we are measuring the X operator on each of the two or four qubits, hence we use the controlled-not (X) gate

In Figure 2a, we started with an initial state of the ancilla qubit which is $|0\rangle$. The initial combined state of the system is $|0\rangle \otimes |\psi_{in}\rangle$ in which $|\psi_{in}\rangle$ is a general state over $|q_1\rangle$ and $|q_2\rangle$. Then, we apply the Hadamard gate. After applying the Hadamard gate, the initial combined state of the system, $|0\rangle \otimes |\psi_{in}\rangle$, becomes transformation 1:

$$|0\rangle |\psi_{in}\rangle \xrightarrow{\text{Hadamard}} \frac{1}{\sqrt{2}} (|0\rangle + |1\rangle) |\psi_{in}\rangle \quad (1)$$

After the Hadamard gate, we have two CNOT gates. Once we apply the CNOT gates sequentially, we have the transformation of 1 to 2:

$$\frac{1}{\sqrt{2}} (|0\rangle + |1\rangle) |\psi_{in}\rangle \xrightarrow{\text{CNOT's}} \frac{1}{\sqrt{2}} (|0\rangle |\psi_{in}\rangle + |1\rangle XX |\psi_{in}\rangle) \quad (2)$$

After sequential CNOT gates, we again apply the Hadamard gate and then we have the transformation of 2 as follows:

$$\begin{aligned} & \frac{1}{\sqrt{2}} (|0\rangle |\psi_{in}\rangle + |1\rangle XX |\psi_{in}\rangle) \xrightarrow{\text{Hadamard}} \\ & \frac{1}{2} |0\rangle (|\psi_{in}\rangle + XX |\psi_{in}\rangle) + \frac{1}{2} |1\rangle (|\psi_{in}\rangle - XX |\psi_{in}\rangle) \end{aligned} \quad (3)$$

The last step of the circuit is measuring the ancilla qubit. After the measurement, if :

$$\begin{aligned} \text{ancilla} = |0\rangle & \Rightarrow \frac{|\psi_{in}\rangle + XX |\psi_{in}\rangle}{2} \cong |\psi_{out}\rangle \\ \text{ancilla} = |1\rangle & \Rightarrow \frac{|\psi_{in}\rangle - XX |\psi_{in}\rangle}{2} \cong |\psi_{out}\rangle \end{aligned} \quad (4)$$

where \cong means up to a renormalization factor. Now, let us look at the symmetries of $|\psi_{out}\rangle$
If:

$$\begin{aligned} \text{measured } |0\rangle & \Rightarrow XX |\psi_{out}\rangle = XX \left(\frac{|\psi_{in}\rangle + XX |\psi_{in}\rangle}{2} \right) \\ & = \frac{XX |\psi_{in}\rangle + |\psi_{in}\rangle}{2} \\ & = |\psi_{out}\rangle \end{aligned} \quad (5)$$

If:

$$\begin{aligned}
\text{measured } |1\rangle \Rightarrow XX |\psi_{out}\rangle &= XX \left(\frac{|\psi_{in}\rangle - XX |\psi_{in}\rangle}{2} \right) \\
&= \frac{XX |\psi_{in}\rangle - |\psi_{in}\rangle}{2} \\
&= - \left(\frac{|\psi_{in}\rangle - XX |\psi_{in}\rangle}{2} \right) \\
&= - |\psi_{out}\rangle
\end{aligned} \tag{6}$$

Hence, dependent on the measurement result, we have projected our state into eigenstates of the XX operator with eigenvalues $+1$ or -1 , with the ancilla measurement result dictating which eigenstate we have projected into. If the input was already in an eigenstate with eigenvalues $+1$ or -1 , we will simply obtain a measurement result on the ancilla that indicates the parity of the input state, without changing the state itself. We therefore have the parity information of the multi qubit system by using CNOT gates and a one-body measurement, (CNOT's + M_{pp1}).

Multi-body measurements are used in different aspects of quantum information/computation. In QEC, stabilizer measurements are the important examples of multi-body measurements, that occur over the operators that define the stabilizers of the QEC code. However, for example, instead of making direct XX parity check measurement, called M_{pp2} , we perform this measurement by using CNOT's + M_{pp1} and single qubit rotations. Here M_{pp2} refers to the fact that the operator we are measuring, XX , is a Pauli operator with weight two.

In quantum computation, single-triplet readout is also a multi-body measurement over 2 qubits. By applying singlet-triplet readout, we can know if we have a singlet or triplet state of the electron. However, we are not using it to measure the parity of a multi-qubit Pauli operator, so we do not classify it as M_{pp2} .

When we measure a qubit, we are in fact performing a one-body parity measurement and we are then able to define the states uniquely. However, when we have multiple qubits and we try to measure these multi-qubit systems, our goal is to restrict the global space into subspaces where the symmetry of the measured operator is enforced. For instance, we will take Figure 2a as an example. If we take the input state as,

$$|\psi_{in}\rangle = \alpha |00\rangle + \beta |01\rangle + \gamma |10\rangle + \delta |11\rangle \tag{7}$$

where, α, β, γ and δ are arbitrary complex amplitudes that define a unique state in

this four dimensional Hilbert space. Now, if we restrict the space by enforcing a symmetry, i.e., by running the circuits in 2a, prior to measurement of the ancilla, the three qubits are in a state namely $|\psi_{bm}\rangle$, bm is before measurement, can be written as in Equation 8.

$$|\psi_{bm}\rangle = |0\rangle \left(\frac{1}{2}(I + XX) |\psi_{in}\rangle \right) + |1\rangle \left(\frac{1}{2}(I - XX) |\psi_{in}\rangle \right) \quad (8)$$

Here $|0\rangle$ and $|1\rangle$ are the states of the ancilla qubit. We know that measuring the ancilla state will project the state into an eigenstate of XX . If we assume that we measure the ancilla in $|0\rangle$ and project our state into the +1 eigenstate of XX , we can write our output state $|\psi_{out}\rangle$ as,

$$|\psi_{out}\rangle = \frac{1}{2} (\alpha |00\rangle + \beta |01\rangle + \gamma |10\rangle + \delta |11\rangle) + \frac{1}{2} (\alpha |11\rangle + \beta |10\rangle + \gamma |01\rangle + \delta |00\rangle) \quad (9)$$

By grouping them;

$$|\psi_{out}\rangle = (\alpha + \delta) \left(\frac{|00\rangle + |11\rangle}{2} \right) + (\beta + \gamma) \left(\frac{|01\rangle + |10\rangle}{2} \right) \quad (10)$$

We can rewrite Equation 10 as follows:

$$\begin{aligned} \frac{(\alpha + \delta)}{\sqrt{2}} &= \alpha' \text{ and } \frac{(|00\rangle + |11\rangle)}{\sqrt{2}} = |\hat{0}\rangle \\ \frac{(\beta + \gamma)}{\sqrt{2}} &= \beta' \text{ and } \frac{(|01\rangle + |10\rangle)}{\sqrt{2}} = |\hat{1}\rangle \end{aligned} \quad (11)$$

As a result, we have:

$$|\psi_{out}\rangle = \alpha' |\hat{0}\rangle + \beta' |\hat{1}\rangle \quad (12)$$

which is effectively a new qubit. Hence, by enforcing a symmetry on our original two-qubit system, we have reduced it to an effective one qubit system, where our new basis states, $\{|\hat{0}\rangle, |\hat{1}\rangle\}$, are both +1 eigenstates of XX . Making multi-body parity measurements enforces the symmetry of the system and reduces the number of degrees of freedom. A two-body parity measurement over a two qubit system reduces the result into effective one-qubit. This generalises, for an N qubit system, every symmetry we enforce, by performing a measurement of an arbitrary operator, reduces the effective number of qubits in the system by one [17][18].

3. How do Gate Primitives Influence the Code Threshold?

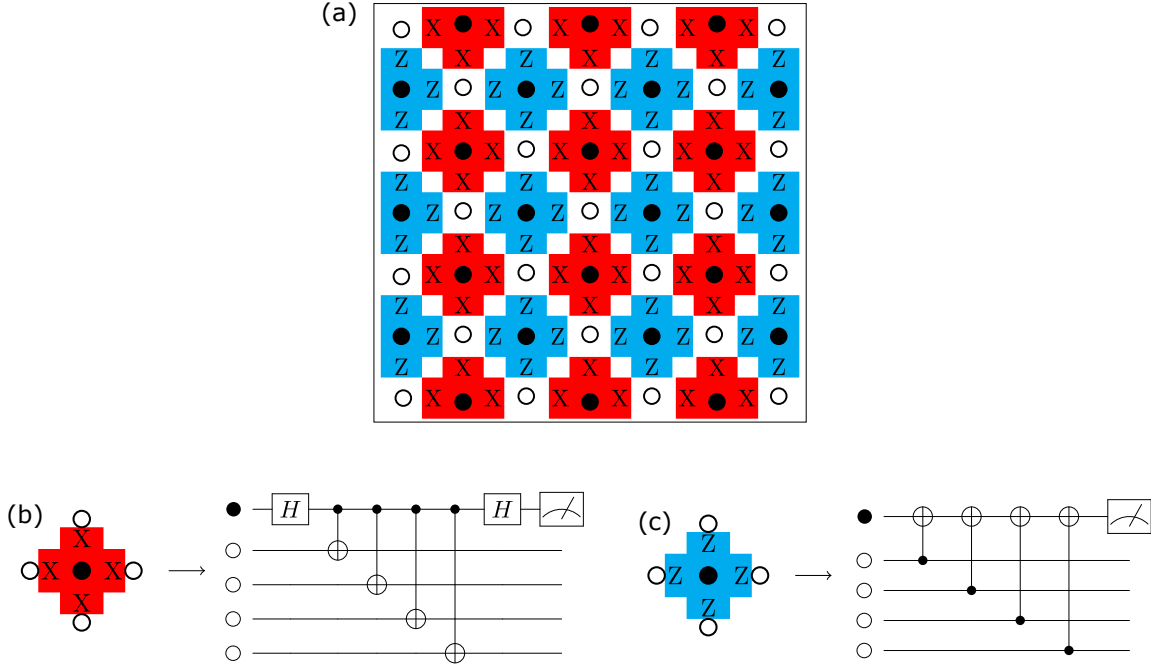


Figure 3: Surface Code Structure. Data qubits are the empty circles and syndrome qubits are the filled circles. In the surface code, we have 2 type of stabilizers, the four-body $XXXX$ and the four-body $ZZZZ$. b) the $XXXX$ stabilizer and the Circuit definition of an $XXXX$ parity measurement - $XXXX$ stabilizer - in the Surface code. c) the $ZZZZ$ stabilizer and circuit definition of a $ZZZZ$ parity measurement - $ZZZZ$ stabilizer - in the Surface Code.

Gate primitives - and the noise models that best reflect these primitives - can influence the threshold of the QEC scheme. They can increase or decrease the threshold, depending on the underlying assumptions about which gates are used as ‘native’. In this section we will look at the threshold values for different assumptions about how QEC stabilisers are measured.

We are going to give an example of the surface code since it is extremely well studied [9][13][19]. Before going through the noise models, let us remember some of the key points of the surface code. The Surface code is placed under topological codes since the stabilizers are local where information is stored globally. The qubits are located on the two dimensional square lattice which encodes a single logical qubit [20][21]. Length of logical Pauli Operators is equal to d which is the distance

of the surface code and the code is able to detect up to $d/2$ errors. Figures 3b and 3c show the two circuits of the surface code that are used repeatedly to perform error correction. The error behaviour of the code depends strongly on how these circuits are physically implemented.

3.1. Code Capacity Noise Model

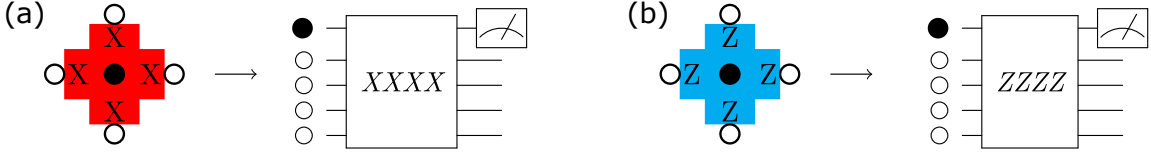


Figure 4: Code Capacity Noise model for $XXXX$ and $ZZZZ$ stabilizer $-M_{pp4} = ZZZZ$ (or $XXXX$) gate + single qubit measurement. The empty circles represent the data qubits and the filled circles represent the ancilla qubits

In this model, it is assumed that the error rate of the syndrome bit is zero so the error syndrome of the surface code needs to be measured only once since it is perfectly reliable. The Code capacity noise model assumes that we can measure the stabilizers depicted in Figure 3b and Figure 3c in one step perfectly without using the circuits which are constructed by using separated gates. According to this model, we have a special unitary gate and we are able to measure the stabilizer of the surface code with this special unitary as it shown in Figure 4. The Code capacity noise model allows us to have error on one of the data qubits, which are the empty circles in Figure 4. This model is actually a direct measurement - without using separated gates - of a four dimensional Pauli. Hence, this is M_{pp4} . We can generalize the formulation of M_{pp4} as Equation 13 in the same way in [14]:

$$M_{pp4} = \{I, X, Y, Z\}^{\otimes 4} \times \{flip, noflip\} \quad (13)$$

The error model, defined in Equation 13, allows us to differentiate between two types of errors: quantum errors and classical errors. The left side of Equation 13 represents the quantum errors and it allows us to have one Pauli error on one of the data qubits. The right side of Equation 13 represents the classical error and it allows us to have one classical bit flip error which is the bit flip error on the classical measurement

result on the ancilla qubit. The Code capacity noise model assumes the existence of perfect M_{pp4} without using individual one and two qubit gates and it assumes that the classical parity measurement always results in a *no flip* outcome. The threshold value for this noise model is $\approx 10\%$ [13]. The accuracy threshold for the code capacity noise model is differentiated with what is sometimes referred to as single shot [22]. A single shot error correction technique is where we have the possibility of errors in the actual parity measurement (i.e. the classical bit of information that tells us what parity the qubits are projected to is not reflective of what the quantum information is actually projected to) and we utilise other redundancies in the code to detect and correct for these events. This is in contrast to the traditional way to correct for these types of errors, which requires multiple measurements of the same operator [23]. However, in the code capacity noise model, we do not have errors to correct that occur outside of the data qubit, nor any circuit mechanisms to spread a data qubit error to a subsequent measurement error. There is another single shot which experimentalists use for readout [24][25] in which they can read the outcome of the measurement of a qubit without requiring any averaging. But this single shot readout does not aim to correct errors, so the single shot readout and single shot in QEC [23] also differ.

3.2. Phenomenological Noise Model

In this noise model, we assume the same noise model as in the Code capacity noise model, but now we re-introduce the *flip*, *no flip* error occurring on the classical bit of the parity measurement. We can have the Pauli errors on the data qubits and the classical bit flip error on the classical measurement result of the ancilla qubit with probability p . However, the propagation induced by any circuit that is used to realise these measurements is ignored. This model assumes that we have M_{pp4} but this M_{pp4} is imperfect and so must be repeated multiple times. The threshold value for this model is $\approx 3\%$ [13].

3.3. Biased Noise Model

In this noise model, one of the Pauli errors occurs with a higher rate whereas the other two occurs with a lower rate. For example it is commonly studied that Pauli Z errors occur with a higher rate compared to the Pauli X and Pauli Y errors [26][27][28][29][30]. This model is most appropriate for superconducting

qubits [31], trapped ions [32] and quantum dots [33]. Another candidate for this model is semiconductor spin qubits, for example silicon spin qubits [34][35]. These spin qubits are more susceptible to Z errors compared to superconducting qubits due to the presence of colored noise. As a result of the colored noise, there is a distinction between the values of T_2^* and $T_2^{\text{Hahn-Echo}}$. Hence $T_2 = T_2^* + T_2^{\text{Hahn-Echo}}$. In contrast, superconducting qubits experience white noise and therefore have a single T_2 value. Recently, it was shown that the Surface code can have an ultrahigh threshold with biased Pauli Y error instead of Pauli Z error [36]. Furthermore, it was discovered that we can have a 50% threshold for highly biased noise [37]. The problem here, is how much is this noise biased. At which conditions can we access that much biased noise for that high threshold value?

3.4. Circuit Based Noise Model

The Circuit based noise model is currently the most accurate, given how quantum computers are actually constructed. This model uses a one-body measurement gate, M_{pp1} and standard single and two-qubit gates. In this model, we model single qubit gates - this includes identity gates, initialisations and measurements - as being applied perfectly, followed by X , Y or Z errors with respective probabilities. Similarly, two qubits gates are modelled as perfect, followed by errors chosen from the 15 possible combinations from the set, $\{I, X, Y, Z\}^{\otimes 2}$. So to construct multi-body measurements - M_{pp4} - we construct a parity check circuit that consists of four two-qubit gates, two-single qubit gates and ancilla initialisation and ancilla measurement. This model is discussed in Section 5 in detail. The threshold of this model can change between 0.5% [13] and 0.7% depending on the specifics of the parity check circuit construction [14].

4. Honeycomb Code

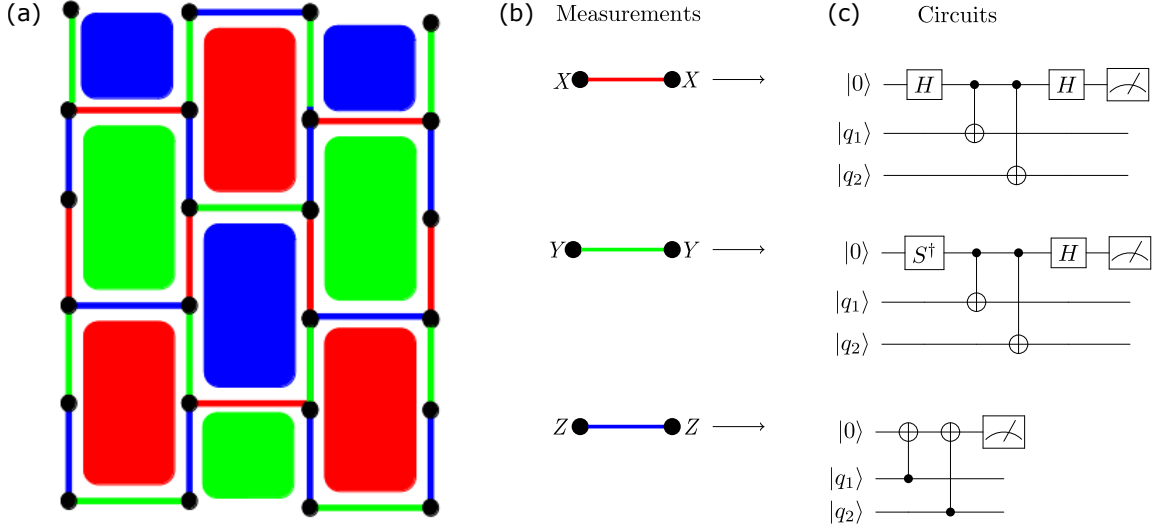


Figure 5: Honeycomb code a) General structure of the Honeycomb code. Black dots represents physical qubits. When we multiply the blue edges and the red edges, we get the green face which is 6 body Y stabilizer. When we multiply the blue edges and the green edges, we get the red face which is 6 body X stabilizer. When we multiply the red edges and the green edges, we get the blue face which is 6 body Z stabilizer. b) Measurements for the Honeycomb Code. Honeycomb code requires two body parity check: XX , YY and ZZ c) Circuit equivalents for XX , YY and ZZ parity measurement via traditional method which is single qubit gates plus two qubit gates plus M_{pp1} .

Unfortunately, for $M_{pp} > 2$, Hamiltonians are generally not physically realisable since they require the interaction terms to be more than two-body [38][39][40]. For that reason, we are not able to implement the code capacity noise model and the phenomenological noise model directly and instead turn to circuit constructions and noise models. The only way to implement the Surface code, in an architecturally realistic manner, is to use the Circuit Based Noise Model which exhibits a lower threshold, increasing the burden on hardware manufacturing.

In 2020, the Honeycomb code [41], a variant of Floquet codes [42], was introduced as a novel quantum error correction (QEC) code § The Honeycomb code stands as one of the more recent advancements in topological code constructions. It

§ This code was originally introduced by Kitaev in 2006[39], but its use as a QEC code was demonstrated in the work[41].

involves qubits positioned on a 2D lattice, forming a fixed hexagonal configuration. The distinguishing feature of the Honeycomb code, in contrast to the surface code, is its reliance on two-body parity checks, specifically XX , YY , and ZZ measurements, instead of requiring $XXXX$ and $ZZZZ$ measurements. Figure 5c provides the equivalent circuit for performing XX and ZZ parity check measurements in the Honeycomb code. It was also shown that this code exhibited comparable thresholds to the surface code [43], in contrast to Gauge codes which can be realised using two-body parity checks, but whose stabilisers are generally much higher weights [44]. Since the Honeycomb code requires only two-body parity measurements, M_{pp2} , which may be achievable experimentally in some systems naturally. In [14], Gidney and Fowler showed that if considered a situation where a natural M_{pp2} measurement is available from the hardware, such that error modelling essentially mirrors a phenomenological noise model, where a perfect multi-qubit measurement is applied, followed by the error mapping:

$$\{I, X, Y, Z\}^{\otimes 2} \times \{flip, noflip\} \quad (14)$$

with probability, p , then the threshold of the Honeycomb code was found to be approximately 2%. This threshold is commensurate with the phenomenological threshold for the surface code, but unlike the surface code, some hardware systems may have the possibility of realising M_{pp2} operations, while it is unlikely that a natural M_{pp4} measurement will be found in any current hardware systems.

This means that if we can have a natural two-body measurement that satisfies the error model of Gidney and Fowler, we will have a three times higher threshold for the Honeycomb code while maintaining a 2D Nearest-Neighbour hardware architecture. Furthermore, the latest study by Gidney [45], shows that if we run the surface code by using natural two-body measurements, the threshold of the surface code will be similarly increased.

The clear question is: how does an experimental system verify that a possible natural M_{pp2} operation satisfies the assumptions used in the above analysis? We first explain an analysis workflow that can map a standard experimental process matrix to an equivalent QEC-specific error model, necessary to check if the error behaviour of a real system matches the assumptions of a threshold analysis. We then construct and verify a native gate set designed specifically for QEC. Rather than targeting standard gates such as CNOTs, we target the higher dimensional unitaries needed to realise these syndrome extraction circuits. We will call this native gate set the

single-step parity check gate set. We then proceed to apply this technique to the two-qubit parity check circuits necessary for the implementation of the Honeycomb code. We present the single-step parity check gates in the context of spin qubit systems.

5. Understanding the Current Way of Constructing Parity Check Circuit and Its Drawback in the Context of QEC

The current standard method for constructing multi-body measurements involves creating entanglement between the data qubits and the ancilla qubits by applying controlled-gates, such as the CNOT (CX) gate for the X parity measurement, and then performing a one-body measurement on the ancilla qubit. The ancilla is crucial in this process, as without it, the measurement result will not provide us with the parity information. While this works in theory, it is expensive in the lab and we may be able to do better as natural two qubits measurements are possible in some systems. Each layer of gates added results in a decrease in the total fidelity of the quantum circuit. To show this decrease, we will analyze Figure 2a in detail by using the experimental data from [16] and we will calculate the accumulated errors in the circuit in terms of stochastic Pauli channels. This calculation assumes that we apply each of the operators just before making the measurement and model the every imperfect gate as perfect gates plus some error.

5.1. Preliminaries

- (i) Superoperators represent a linear map between initial and final density matrices of the system. They are the mathematical representations which bring one density matrix to another. The unitary evolution of a density matrix is defined by Equation 15 where U is the unitary matrix and its dimension is $2^n \times 2^n$, n is the number of qubits, ρ_i is the initial state of the system and ρ_f is the final state of the system after this unitary is applied.

$$\rho_f = \mathcal{E}(\rho_i) = U\rho_iU^\dagger \quad (15)$$

where \mathcal{E} describes a quantum channel.

Now, there exists a linear representation of \mathcal{E} due to Choi-Jamarkowski which brings $|\rho_i\rangle\rangle \mapsto |\rho_f\rangle\rangle$ and its representation based on the vectorization of the

density matrix with respect to the column basis: [46].

$$U \otimes U^\dagger |\rho_i\rangle\rangle = |\rho_f\rangle\rangle \quad (16)$$

Dimensions of the Superoperators are equal to $2^{2n} \times 2^{2n}$ where n is the number of qubits and $|\cdot\rangle\rangle$ represents vectorization.

- (ii) Equation 15 is the special case where we have applied the unitary U in the absence of environmental noise. However, in the presence of imperfect gates or environmental noise, Equation 15 will not be enough to represent the imperfections. In this case, we will need a more general mapping to represent our system. Kraus operators are the most general representation of our system in the presence of noise and they represent both the systematic gate errors and the errors induced by environmental decoherence [18]. Then, the density matrix can be written as

$$\rho_f = \mathcal{E}(\rho_i) = \sum_{k=1}^N A_k \rho_i A_k^\dagger, \quad (17)$$

with

$$\sum_{k=1}^N A_k^\dagger A_k = 1, \quad (18)$$

where $N \leq 2^{2n}$ and $\{A_k\}$ are the set of Kraus operators which replace the unitary in Equation 15. The Kraus operators, $\{A_k\}$, are not necessarily unitary operators, hermitian operators or invertible. If $N = 1$, this means that we have the ideal case and this brings us back to the Equation 15 where A_k is U . Equation 18 is called the completeness condition if the map is trace-positive, TP. Note that since the quantum channels considered here map the system to itself, we only consider Kraus operators to be square matrices.

- (iii) χ - Process matrix

When we write Kraus operators in the Pauli basis, in other words, A_k is extended in terms of Pauli operators, then we will have $A_k = \sum_{j=1}^{d^2} a_{jk} P_j$ where $P_j \in P^{\otimes n}$ and $P = \{I, X, Y, Z\}$. If we write that in Equation 17, then we will have:

$$\rho_f = \mathcal{E}(\rho_i) = \sum_{j=1}^{d^2} \chi_{jk} P_j \rho_i P_k \quad (19)$$

where $\chi_{jk} = \sum_i a_{ij} a_{ik}^*$. The χ matrix is a complex-valued matrix with dimension $2^{2n} \times 2^{2n}$ and is a complete map of ρ_f . The χ matrix is also the output of process tomography[47].

- (iv) The Pauli Transfer Matrix (PTM), which is shown as R in literature [46][47][48][49], is another useful representation of a quantum channel and an outcome of Gate Set Tomography[47][50]. It is defined by the vectorization of a quantum channel in the Pauli basis and it can be written as:

$$(R_\varepsilon)_{ij} = \frac{1}{d} \text{Tr}\{P_i \mathcal{E}(P_j)\} \quad (20)$$

Here, P_j 's represents ordering in the strings of Pauli operators, i.e $\{I, X, Y, Z\}$. The PTM, R , is the special case of Superoperators where the vectorization is made in the Pauli basis. One notable advantage of using the Pauli Transfer Matrix, R , is its exclusive utilization of real elements. Furthermore, R facilitates the straightforward determination of whether a quantum operation is trace-preserving or unital. It is also noteworthy that for any Clifford operation, each row and column of R with unit magnitude contains a single non-zero element. The PTM makes it easy to evaluate the result of multiple gates acting in succession. The process matrix does not have this property. This is why the output matrices of Gate Set Tomography(GST) are PTM[50].

- (v) The Density Matrix in the context of QEC:

We shall commence the construction of the density matrix for a single qubit. For the density matrix of multi-qubit systems, we refer the reader to the Appendix. A-.3A-.4). In this case, the dimensions of Kraus operators will be 2×2 . Once we found the Kraus operators, they can be written in terms of Pauli matrices as in Equation 21, since every complex 2×2 matrix can be written by Pauli Matrices ||.

$$A_k = C_0 I + C_1 X + C_2 Y + C_3 Z \quad (21)$$

If the Kraus operators in Equation 17 are decomposed as in Equation 21, then we have:

$$\rho_f = \sum_{a \in M} \sum_{b \in M} a \rho_i b^\dagger \quad (22)$$

where $M = \{C_0 I, C_1 X, C_2 Y, C_3 Z\}$.

Suppose the map described by Equation 22 acts on a qubit that is part of a larger QEC-encoded system. We will now explore the observable effect of this

|| Also every $2^n \times 2^n$ matrix can be written as a linear combination of the tensor products of n Pauli matrices. The total number of independent tensor products of Pauli matrices is 2^{2n}

mapping when we run a quantum error correction cycle. For this purpose, let us consider an error model, such as the one given in Equation 23:

$$\rho_f = p_i \rho + p_x X \rho X + p_{xy} X \rho Y \quad (23)$$

Here ρ represents a qubit, while X and Y represent the physical error on the qubits in the code block. An ancilla block, represented by the density matrix ρ_0^E is coupled to the system and the quantum error correction unitary which is called U_{QEC} is run:

$$U_{QEC}(\rho_f \otimes \rho_0^E)U_{QEC}^\dagger = p_i \rho \otimes |E\rangle \langle E| + p_x X \rho X \otimes |E_x\rangle \langle E_x| + p_{xy} X \rho Y \otimes |E_x\rangle \langle E_y| \quad (24)$$

Here, $|E\rangle$, $|E_x\rangle$ and $|E_y\rangle$ represent the three orthogonal syndrome states of the ancilla qubit and they are used to detect errors on the qubits. Now, when the ancilla qubit is measured, the system will be collapsed to one of the two states in Equation 25

$$\rho_f \Rightarrow \frac{\langle E | \rho | E \rangle |E\rangle \langle E|}{\text{Tr}(\rho |E\rangle \langle E|)} \quad \text{and} \quad \rho_f \Rightarrow \frac{\langle E_x | \rho | E_x \rangle |E_x\rangle \langle E_x|}{\text{Tr}(\rho |E_x\rangle \langle E_x|)} \quad (25)$$

The off-diagonal term, in this case the $p_{xy} X \rho Y$ term in the error model, is never observed. After the measurement of the ancilla, we have two possible states which are shown in Equation 26

$$\begin{aligned} &\rho \otimes |E\rangle \langle E| \text{ with probability } p_i \\ &X \rho X \otimes |E_x\rangle \langle E_x| \text{ with probability } p_x \end{aligned} \quad (26)$$

The off-diagonal term is eliminated because we are about to make a measurement in the E , E_x basis and the measurement result will collapse one of the diagonal terms. Although it was written in [18], it is once more worth noting that not only the off-diagonal term is eliminated but the final density matrix is collapsed to clean codeword states with bit-flip errors. Here, we do not use the twirling method which is a way to convert the off-diagonal terms of the matrix into the diagonal terms[51][52]. In quantum computation, there are some protocols that use twirling, such as purification protocols [53][54][55]. However, when we write errors in terms of stochastic Pauli channels, we let unitaries evolve until the measurement is done. This is why, when we calculate the effective errors in

the context of QEC, we only care about diagonal elements and we ignore off-diagonal elements. Hence, we are finding the diagonal elements of the χ matrix and we are writing the Kraus operators in terms of these diagonal elements of the χ matrix. It is true that we are losing the information by ignoring the off-diagonal terms. In Equation 22, once cancelling the off-diagonal elements, we have,

$$\rho_f = p_i I \rho_i I + p_x X \rho_i X + p_y Y \rho_i Y + p_z Z \rho_i Z \quad (27)$$

where $p_i = (|C_0|)^2$, $p_x = (|C_1|)^2$, $p_y = (|C_2|)^2$, $p_z = (|C_3|)^2$. This formula represents effective errors in the context of QEC for 1 qubit. As an illustration, in the case of implementing the identity gate, the coefficient p_i serves as an indicator of the gate's efficacy. A value of $p_i = 1$ signifies the perfect implementation of the identity gate. The Equation 27, can be written for any state and in QEC, the errors in the quantum channel are analyzed after the application of the desired unitary. Because of that, to utilize the Equation 27 in a more general way, the ρ_i is replaced with ρ_g where $\rho_g = U \rho_i U^\dagger$ and the U is the desired unitary that we want to implement. Then, the Equation 27, becomes Equation 28:

$$\rho_f = p_i I \rho_g I + p_x X \rho_g X + p_y Y \rho_g Y + p_z Z \rho_g Z \quad (28)$$

In Equation 28, the p_i represents the probability of having no error. We define it as the perfection rate. If $p_i = 1$, we are in the ideal case with no error and we turn back to Equation 15. For all the other values of p_i , we use the Kraus decomposition. The coefficients p_x , p_y and p_z are, now, the probability of having X errors, the probability of having Y errors and the probability of having Z errors, respectively. We start with the experimental data, in our case the experimental data is the PTM matrix, and we end up with Equation 28. This result is the important conclusion of the section. If we want to determine error rates subsequent to the implementation of a unitary operation within the framework of Quantum Error Correction (QEC), every operation performed in the laboratory will be denoted as Equation 28. This equation represents a whole process and the coefficient p_i in the equation represents the perfection of the operation that can't be written simply as the fidelity. For example, if we have 99% fidelity for a specific operation, this does not mean that the coefficient $p_i = 0.99$. To find the coefficient p_i , we need to do the whole workflow: we first take the experimental process matrices of the system and find

the Kraus operators. Subsequently, we then write the Kraus operators in terms of stochastic Pauli channels and determine the value of coefficient p_i , which is the perfection rate and it is not equal to fidelity. It is less than the fidelity. Neither the fidelity means the perfection rate, nor the infidelity means the error rate. To finding the error rate, we need information beyond the fidelity [56]A-.2. We give a complete tutorial in the supplementary material regarding this process. If we take Figure 6 as an example and calculate the probability of experiencing certain errors when gates are applied to qubits, the equation which represents the perfection of the operator will be Equation 29. The detailed derivation of Equation 29 is shown in A.4.

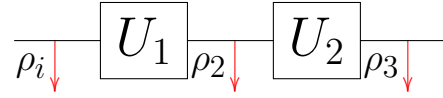


Figure 6: A one qubit circuit example which will be used to calculate effective errors in the context of QEC. At the beginning, the circuit will have ρ_i . After applying a U_1 gate, the density matrix will become ρ_2 and the final density matrix will be ρ_3 which can be written as ρ_f .

$$P_I = p_{i2}p_{i1} + p_{x2}p_{x1} + p_{y2}p_{y1} + p_{z2}p_{z1} \quad (29)$$

The value P_I is the perfection rate for the whole circuit and it represents the final succession rate after all of the accumulated errors in the widget. The important point is, that P_I is not just the multiplication of perfection rates p_i . The cancellation terms also contribute to P_I since $X \otimes X = I$, $Y \otimes Y = I$ and $Z \otimes Z = I$. We will call P_I as the perfection rate of the widget.

5.2. Analyzing the XX Parity Check Circuit from Experimental Data in the Context of QEC

In this part of the study, we use data from [16] to show how the output perfection rate decreases for XX parity check circuit which is the smallest parity check measurement that we can use to implement a topological error correcting code. This study showcases the universal quantum logic operations performed on a silicon nanoelectronic device utilizing a pair of ion-implanted 31P donor nuclei. This device, consisting of two phosphorus and one electron system, is henceforth referred to as the ‘2P1e’ device. Researchers precisely characterized the quantum operations by

using Gate Set Tomography [47][50]. They achieved one-qubit gates with average gate fidelities up to 99.95(2)%, two-qubit gates with an average gate fidelity of 99.37(11)% and two-qubit preparation/measurement fidelities of 98.95(4)%. These results indicate that nuclear spins in silicon are close to the performance required by fault-tolerant quantum processors. This work presents the best result in the field in terms of the fidelity of the operations on these qubits.

Here, we will demonstrate, for the first time, the decrease in the perfection rate of the parity check circuit when utilizing one-body measurement (M_{pp1}) with 1- and 2-qubit gates.

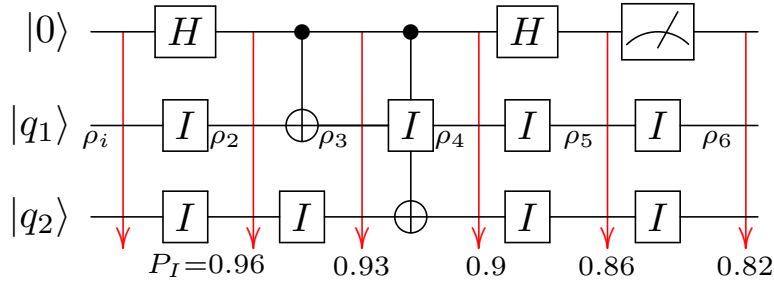


Figure 7: Analysis of the XX parity check circuit in terms of QEC. The circuit depth is 6 and we have 6 steps to calculate in the widget. We first start with ρ_i . Each step that we apply the gates, the value of having no error in the channel (P_I) decrease since the errors accumulate to the next step of the circuit

Figure 7 shows the decrease of perfection rate for the XX parity check measurement which is constructed by the circuit based model. Another important point is the identity gates. When we apply a single qubit gate on a multi-qubit circuit, the qubits which have no applied gate should stay stable and this is represented by identity gates. They are generally the most difficult gates in a quantum system since it is hard to keep the system unperturbed in such noisy environments.

As each step progresses in Figure 7, errors accumulate. Initially, the system is in state ρ_i . Then, a Hadamard gate is applied to the first qubit and an identity is applied to the other two, resulting in state ρ_2 from ρ_i . The final density matrix for ρ_2 is calculated, in terms it of having experienced certain errors in a QEC block, resulting in a perfection rate of 0.96. The next step, ρ_3 , includes errors from not only CNOT and identity operations, but also from ρ_2 . When the process continues, the

final perfection rate is found to be 0.82. The perfection rate between the application of the first operation - in this case, the Hadamard gate on the ancilla qubit and the identities on the $|q_1\rangle$ and $|q_2\rangle$ - and the measurement operation decreased by 14%, indicating a 14% increase in errors in the circuit. Below, we will explain our algorithms for finding the perfection rate:

The Algorithm

The algorithm receives the experimental data as its input, and subsequently delivers the two key performance indicators for the quantum circuit: the perfection rate and the total accumulated error rate. In the interest of convenience, our algorithm has been decomposed into three distinct phases:

- Finding Kraus Operators from GST:
- Finding Errors in the Context of QEC
- Calculating the perfection rate of the whole quantum circuit

The initial stage of the algorithm involves specifying the type of the matrices. In case of GST, the suitable format is the PTM and from the GST experiment, $\pi/2$ and CNOT gate matrices are constructed and analysed. The important thing here is to correctly classify the matrix type. This can be achieved through the use of libraries such as Qiskit [57] and Qutip [58]. If we do not explicitly specify the matrix type in our code and attempt to analyze the matrix, for example, to check its physicality (that is CPTP: completely positive and trace preserving) using some libraries, directly from the array, we will receive a False output because we did not specify the matrix type. In addition, if we misidentify the matrix type, for example, when the matrix type is a PTM but we mistakenly identify it as a χ matrix in our code, even though the χ matrix is CPTP, we may receive incorrect results when checking the physicality of the matrix due to the incorrect matrix type specification.

Algorithm Error Analysis in the Context of Quantum Error Correction

Phase 1: *Preparation - Finding Kraus Operators from GST*

```

1: Input : Ideal and experimental GST Matrices
2: Output : Kraus List
3:  $M_{full} = M_{GST} * M_{GSTerror}$ 
4:  $M_{PTM} = PTM(M_{full})$ 
5: if  $M_{PTM}$  is Complete Positive matrix  $== True$  then
6:    $list(M_{Kraus}) = Kraus(M_{PTM})$ 
7:   if  $\sum(i)$ , for  $i$  in  $M_{Kraus} == I$  then
8:     return  $list(M_{Kraus})$ 
9:   end if
10: end if

```

In the first phase of the algorithm, we first check if the matrix is completely positive (CP). If it is not a CP matrix, this means that the experimental method used gives a different result than the PTM. In this case, it is recommended to check the output of the experimental method used in the lab, as it may yield different types of output, such as χ matrix. After specifying the type of the matrix correctly, the second step in Phase 1 is to find the Kraus operators. Then we check if we can find the Kraus operators correctly by using the completeness condition Equation 18 and see if this gives us the identity matrix. If the completeness condition gives us the identity matrix, then we satisfy the trace-preserving condition for the quantum channel. After finding the Kraus operators, the second step is to calculate errors in the context of Quantum Error Correction. For finding errors, we write each Kraus operator in terms of Pauli matrices as shown in Phase 2.

Algorithm Error Analysis in the Context of Quantum Error Correction

Phase 2: *Finding Errors in the context of Quantum Error Correction*

```

1: Input : Kraus List
2: Output : Errors
3: i=Pauli0,x=Pauli1,y=Pauli2,z=Pauli3,result=[],N=qubit number
4: procedure COEFFICIENTS(list( $M_{Kraus}$ ),N)
5:   paulis = list(product([i,x,y,z],repeat=N)
6:   spaulis = list(product(["i","x","y","z"],repeat=N)
7:   for kindex,kraus in enumerate(krauslist) do:
8:     for index,pauli in enumerate(paulis) do:
9:       error =  $\frac{1}{2^N}$  Trace((kraus* (TensorProduct(pauli[0],...,pauli[N])))
10:    end for
11:  end for
12:  return result
13: end procedure
14: d = defaultdict(complex)
15: for value, name, order in result do:
16:   d[name] += abs(value) * abs(value)
17: end for

```

After finding the errors, the density matrix was written in terms of effective errors in the context of QEC as in Equation A.25.

Algorithm Error Analysis in the Context of Quantum Error Correction

Phase 3: *Computing the Perfection Rate*

```

1: Input : H = errors for H gate in dictionary format,
2:         I = errors for I gate in dictionary format,
3:         cnot = errors for CNOT gate in dictionary format
4:         meas = errors for measurement in dictionary format
5: Output : Perfection Rate
6: # For the first part of 2 body parity check circuit which corresponds  $H \otimes I \otimes I$ 
7: HII = defaultdict(complex)
8: for nameH, valueH in H.items() do:
9:     for nameI, valueI in I.items() do:
10:        for nameI, valueI in I.items() do:
11:            name = (*nameH *nameI *nameI)
12:            HII[name] = valueH *valueI *valueI
13:        end for
14:    end for
15: end for
16: # For the second part of 2 body parity check circuit which corresponds
     $CNOT \otimes I \otimes I$ 
17: CNOTI = defaultdict(complex)
18: for nameCNOT, valuecnot in cnot.items() do:
19:     for nameI, valueI in I.items() do:
20:        name = (*nameCNOT *nameI)
21:        CNOTI[name] = valuecnot *valueI
22:    end for
23: end for
24: # For the third part of 2 body parity check circuit which corresponds non-
    adjacent CNOT
25: ICNOT = defaultdict(complex)
26: for nameI, valueI in I.items() do:
27:     for nameCNOT, valuecnot in cnot.items() do:
28:        name = ( *nameI *nameCNOT)
29:        ICNOT[name] = valueI * valuecnot
30:    end for
31: end for

```

```

32: # For the last part of 2 body parity check circuit which corresponds measurement
    gate
33: measII = defaultdict(complex)
34: for nameMeas, valueMeas in meas.items() do:
35:     for nameI, valueI in I.items() do:
36:         for nameI, valueI in I.items() do:
37:             name = (*nameMeas *nameI *nameI)
38:             measII[name] = valueMeas *valueI *valueI
39:         end for
40:     end for
41: end for
42: # Calculating Perfection rate at each step
43: perfection rate = sum(HII[k]*CNOTI[k]*ICNOT[k]*
44: HII[k]*measII[k] for k in HII)

```

Here, since we have 3 qubits (2 data qubits and 1 ancilla qubit), all triplet combinations of Pauli matrices should be considered as possible error probabilities and we take into account all the diagonal terms. In this case, we have 64 different coefficients for the density matrix. The perfection value is calculated in Equation A.26 in terms of accumulating errors. Here, each density matrix includes the previous density matrix which has 64 coefficients. Since we have 6 steps in the XX parity check circuit, then at 6th step, we will have 64^6 coefficients and from those 64^6 , once we extracted the coefficient for the dominated term, Equation A.26 was found. Last phase of the algorithm shows how to calculate the perfection rate for XX parity check circuit. The complete code for replicating the results presented in Figure 7, as well as the software for analyzing errors within the context of QEC, can be found in [59].

In summary, [16] has the leading gate fidelities in silicon spins. However, despite those high fidelities, at the end of the two-body parity check circuit, the perfection rate between application of initial and final operations has decreased from 0.96 to 0.82. The question here is why would we lose more than 10%, when we have almost perfect (99.9%) gates in the system? Can't we find a better way to keep the perfection rate as high as possible? For this purpose, we decided to design the

full unitaries directly, instead of using individual gates. We constructed these new unitaries by modifying the universal gate set. These unitaries are fundamental to QEC rather than universal computation. By using these gates which are fundamental for QEC, we can increase the threshold and decrease the experimental challenge to the scalability. We call these gates as single step-parity check gate set. These gates are actually multi-body parity measurement gates. This is described in section 6

6. Single-Step Parity Check Gate Set and M_{pp2}

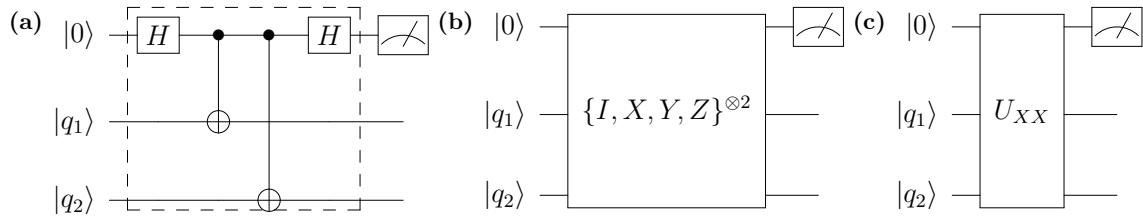


Figure 8: Single-step Parity Check Gate for XX. a) M_{pp2} with current sources. Inside the dashed line represents the custom unitary which we built from. b) Components of natural $M_{pp(2)}$ are described. It represent Equation 14 c) Natural $M_{pp(2)}$ as a widget. We now have a new unitary U_{XX} and one qubit measurement operator.

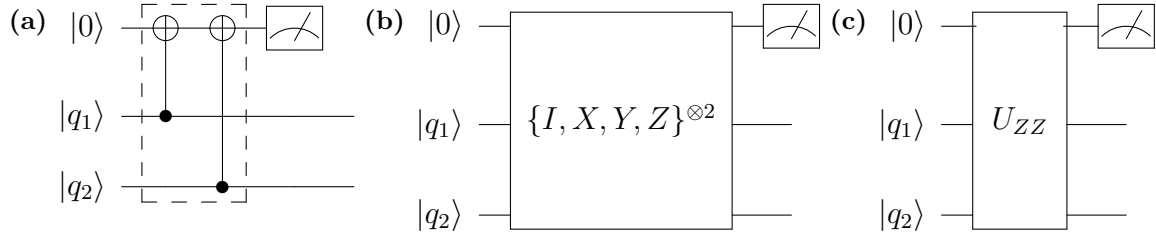


Figure 9: Single-step Parity Check Gate for ZZ. a) M_{pp2} with current sources. Inside the dashed line represents the custom unitary which we built from. b) Components of natural $M_{pp(2)}$ are described. It represent Equation 14 c) Natural $M_{pp(2)}$ as a widget. We now have a new unitary U_{ZZ} and one qubit measurement operator.

The building blocks of quantum circuits are the quantum gates, whereas the building blocks of quantum error correction codes are the parity check circuits. However, the current way of constructing parity check circuits is to utilize the one and two-qubit gates which are the fundamental elements for any quantum circuits.

The idea for single-step parity check gates is to not use the fundamental components of any quantum circuits such as CNOT or single-qubit gates. Instead, we design and optimize the unitary directly. This is a version of pulse optimization where we optimize for the full unitary that is needed for QEC. We use one single unitary to make exactly the same parity check circuit so we are actually using the building blocks of quantum error correction directly without using any other building blocks. In this case, we reduce the number of steps and instead of having six different steps, we just have one single step for exactly the same circuit. From Figure 8a and 9a, the unitaries are found to be Equation 30 and Equation 31 and they belong to the Clifford group. Apart from the new unitary, we now have a new device which can be called a natural M_{pp2} . It is a widget that includes one of those new unitaries, Equation 30 or Equation 31, and a measurement operator. This natural M_{pp2} corresponds to Equation 14. It receives 3 qubits as an input, one of them is used as an ancilla, and it returns the parity information of those two qubits by measuring the ancilla qubit.

In the next part of the study, we will give an example of demonstration of the single step parity check gate and we will explain the structure which is required to build this gate.

$$U_{XX} = \frac{1}{2} \begin{pmatrix} 1 & 0 & 0 & 1 & 1 & 0 & 0 & -1 \\ 0 & 1 & 1 & 0 & 0 & 1 & -1 & 0 \\ 0 & 1 & 1 & 0 & 0 & -1 & 1 & 0 \\ 1 & 0 & 0 & 1 & -1 & 0 & 0 & 1 \\ 1 & 0 & 0 & -1 & 1 & 0 & 0 & 1 \\ 0 & 1 & -1 & 0 & 0 & 1 & 1 & 0 \\ 0 & -1 & 1 & 0 & 0 & 1 & 1 & 0 \\ -1 & 0 & 0 & 1 & 1 & 0 & 0 & 1 \end{pmatrix} \quad (30)$$

$$U_{ZZ} = \begin{pmatrix} 1 & 0 & 0 & 0 & 0 & 0 & 0 & 0 \\ 0 & 0 & 0 & 0 & 0 & 1 & 0 & 0 \\ 0 & 0 & 0 & 0 & 0 & 0 & 1 & 0 \\ 0 & 0 & 0 & 1 & 0 & 0 & 0 & 0 \\ 0 & 0 & 0 & 0 & 1 & 0 & 0 & 0 \\ 0 & 1 & 0 & 0 & 0 & 0 & 0 & 0 \\ 0 & 0 & 1 & 0 & 0 & 0 & 0 & 0 \\ 0 & 0 & 0 & 0 & 0 & 0 & 0 & 1 \end{pmatrix} \quad (31)$$

6.1. Comparison of XX Parity Check (with current sources) and Direct Parity Check in the Presence of Noise

In this section, we will show how the perfection rate differs in the presence of noise between decomposed parity check circuit and single-step parity check circuit. For this purpose, we take the circuits defined in Figure 10. In Figure 10 a, the circuit has four three-qubit gates, namely $HII = H \otimes I \otimes I$, $CNOTI = CNOT \otimes I$, $CNOT_{02}$ which is the CNOT gate between non-nearest neighbour qubits (here, non-nearest neighbour qubits are the ancilla and the second data qubit) and again $HII = H \otimes I \otimes I$, while in Figure 10 b it has one three-qubit gate, namely the U_{XX} gate. Each noisy operator can be modelled by perfect gates plus some errors to be mapped in the circuit. We simulated process matrices such that each channel of each building block of the circuit will have $0.00375_{ch1} \otimes 0.00375_{ch2} \otimes 0.00375_{ch3}$ phase flip error rate in addition to a perfect gate. Then we calculate the average gate fidelity from these noisy channels and we find that each gate in the circuit will have 99% fidelity. Note that if we change the error type, the amount of error required to maintain the same fidelity will also change. The reason for selecting this error type is because phase flip errors are the predominant sources of error for most solid-state hardware systems, as mentioned in Section 3.3, especially in semiconductor spin qubits such as the one described in [16]. On the one hand we have four gates with 99% fidelity and on the other hand we have one gate with 99% fidelity. We apply our workflow to find the perfection rate of each circuit defined in Figure 10.

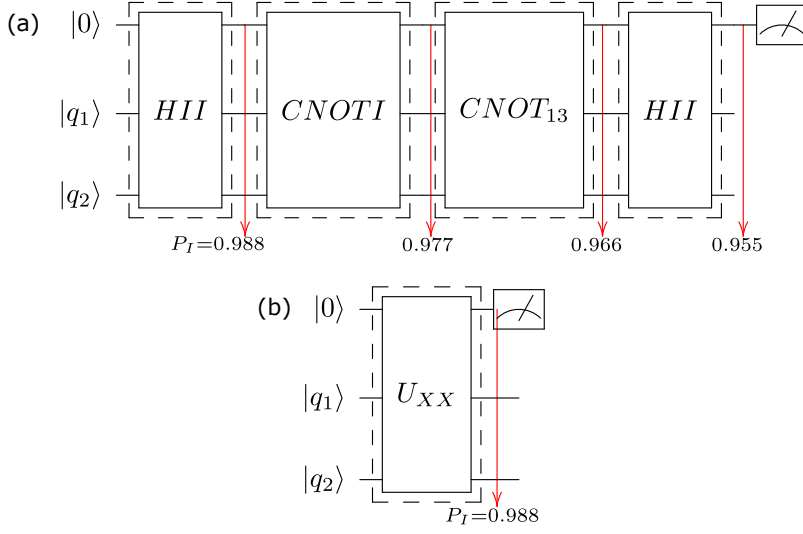


Figure 10: a) A traditional, decomposed, XX parity check circuit. This circuit has four gates, namely HII , $CNOTI$, $CNOT_{03}$ and again HII . b) Defines a direct XX parity check gate with the XX -SSPC gate. We create each of these gates with 99% fidelity.

As it is seen from the result, since the traditional, decomposed, parity check circuit requires four steps (four building blocks), the errors in each step (building block) accumulate. On the other hand, with a SSPC gate, there is no more than one building block so there is no place for errors to accumulate. For this reason, the perfection rate remains high.

As a further illustration, in Figure 11 we show a simulation where each single qubit gate (Hadamard and Identity gate) has 99.43% fidelity, and the CNOT gate experiences the single qubit errors as a tensor product of the amount $(I \otimes X, I \otimes Y \dots)$. We chose this fidelity value because it is the surface code fault-tolerance threshold [9]. To achieve this fidelity, we used an error rate of $p = 0.0085$ for the phase flip error in each single-qubit gate. As depicted in Figure 11, the resulting perfection rate at the circuit's end is 0.9026. This perfection rate is obtained by utilizing gates with the specified fault tolerance error value. To attain an equivalent perfection rate for the XX -SSPC gate, comparable to the decomposed parity check circuit, we can increase the error rate to $p = 0.0329$ for the phase flip error per qubit. Implementing an XX gate with this error rate yields a perfection rate $P_I = 0.9042$, as illustrated in Figure 11b. This example illustrates that if we create the parity check circuit with

a single gate, but with a higher error rates compared to the single- and two-qubit gates, we can still achieve the same perfection rate. This is how we can boost the error threshold value for QEC: instead of using the single- and two-qubit gates, using one unitary which does the same parity check circuit with a single step -SSPC gates. This is due to the absence of error accumulation throughout the circuit.

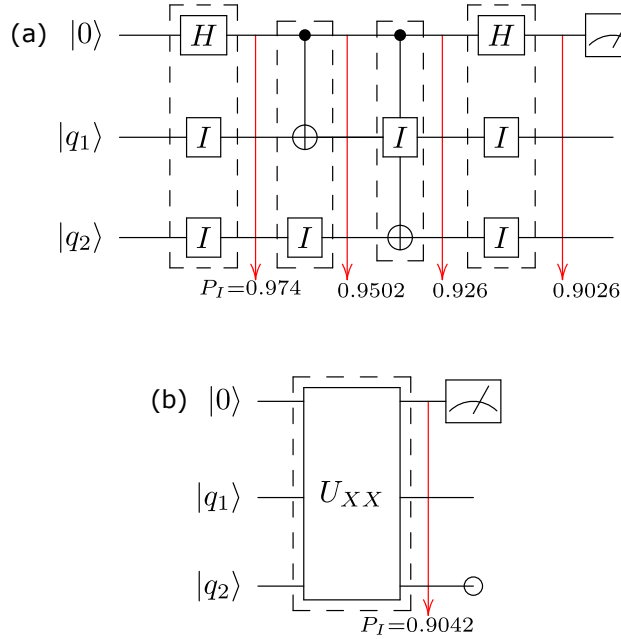


Figure 11: This example shows how we can increase the error threshold by reducing the number of gates in the circuit. Unlike the previous example in Figure 10, we created two circuits with different error rate in order to achieve approximately the same perfection rate. a) A traditional XX parity check circuit. This circuit has Hadamard gate and identity gates as single-qubit gates, and CNOT gates as two-qubit gates. We create each single qubit gate with $p = 0.0085$ per single-qubit gate (99.43% fidelity). Here, we would like to emphasize once again how average gate fidelity can be illusory when attempting to determine the error rate of the gate. The error rate is not equal to infidelity ($1 - 0.9943$). When we calculate the errors in terms of stochastic Pauli channels (in the context of QEC), the total perfection rate at the end of the circuit is $P_I = 0.9026$. b) A direct XX parity check gate with an XX - SSPC gate. For having the same perfection rate as in (a), we increased the error rate up to $p = 0.0329$ per qubit. We then calculated the total perfection rate and found as 0.9042. In (a), because we have many single- and two-qubit gates, the error rate for each qubit per gate is lower than in (b). This is because of the accumulation of errors throughout the circuit. In (b), since we have only one gate, the errors do not accumulate and multiply themselves with the other gates errors. As a result, the acceptable error rate for each qubit is higher than in (a). This is how the error threshold of the QEC can be increased.

6.2. Practical implementation of SSPC Gates

The theoretical discussion in the preceding section illustrates the advantages afforded by implementing parity checks using a single-step M_{pp2} operation instead of breaking it down to a sequence of individual gates. We now illustrate a practical example of how a SSPC gate could be implemented in a real physical system.

Let us consider a three-spin system consisting of an electron spin, acting as the ancilla, and two nuclear spins, acting as the qubits. Their drift Hamiltonian in the laboratory frame takes the general form:

$$\vec{H} = -\gamma_e B_0 \hat{S}_z - \gamma_n B_0 (\hat{I}_{z1} + \hat{I}_{z2}) + A_1 \vec{S} \cdot \vec{I}_1 + A_2 \vec{S} \cdot \vec{I}_2, \quad (32)$$

where $\vec{S} = [\hat{S}_x, \hat{S}_y, \hat{S}_z]$ are the electron spin operators with eigenvectors $\{|\uparrow\rangle, |\downarrow\rangle\}$, $\vec{I}_i = [\hat{I}_x, \hat{I}_y, \hat{I}_z]$ are the nuclear spin operators for nucleus $i \in 1, 2$ with eigenvectors $\{|\uparrow_i\rangle, |\downarrow_i\rangle\}$, A_1 and A_2 are the electron-nuclear hyperfine interactions, γ_e is the electron gyromagnetic ratio, γ_n is the nuclear gyromagnetic ratio, and B_0 is a static magnetic field oriented along the \hat{z} -axis. This Hamiltonian is commonly found in well-studied spin qubit systems such as the nitrogen-vacancy (NV) center in diamond [60], spins in quantum dots [61] and donors in silicon [62]. A Hamiltonian with this structure can be viewed as implementing the smallest possible parity check circuit for the Honeycomb Code, as shown in Figure 12.

We take the specific example of a recent experiment where two ^{31}P nuclear spins were hyperfine-coupled to a common electron (2P1e) and entangled using a geometric CZ gate obtained through a rotation of the electron conditional on the state of the nuclei [16]. The gate fidelities extracted from GST were used in the preceding section to illustrate how gate errors build through a circuit. The numerical parameters of the Hamiltonian are $\gamma_e = -27.97$ GHz/T, $\gamma_n = 17.23$ MHz/T, $B_0 = 1.33$ T, $A_1 = 95$ MHz and $A_2 \approx 9$ MHz. The large separation of energies in the system, whereby the electron Zeeman energy splitting $\gamma_e B_0 \approx 37.2$ GHz is orders of magnitude larger than both the nuclear Zeeman energies $\gamma_n B_0 \approx 22.8$ MHz and the hyperfine interactions, ensures that the eigenstates of the Hamiltonian are almost exactly the tensor products $\{|\uparrow\rangle, |\downarrow\rangle\} \otimes \{|\uparrow_1\rangle, |\downarrow_1\rangle\} \otimes \{|\uparrow_2\rangle, |\downarrow_2\rangle\}$, as shown in Figure 12b.

To implement the ZZ-SSPC gate we add the control Hamiltonian:

$$H_{rf}(t) = -\gamma_e \vec{B}_1 \vec{S} \cos(\omega t) - \gamma_n \vec{B}_1 (\vec{I}_1 + \vec{I}_2) \cos(\omega t) \quad (33)$$

where B_1 is an the oscillating magnetic field strength oriented along \hat{y} . A ZZ-SSPC gate is obtained trivially by applying a bichromatic pulse of B_1 at the frequencies $\omega_{\uparrow\downarrow}$ and $\omega_{\downarrow\uparrow}$ corresponding to the resonance frequencies of the electron spin when the nuclei are in the odd-parity states $|\uparrow\downarrow\rangle, |\downarrow\uparrow\rangle$. This is depicted with the yellow and green lines in Figure 12b. Calibrating the amplitude and duration of the pulse such that the electron undergoes an exact π -rotation implements the CNOT gates depicted in Figure 9c(a). The two frequencies can be applied simultaneously because they both act on the same physical object (the electron). The SSPC gate is then followed by electron readout [24].

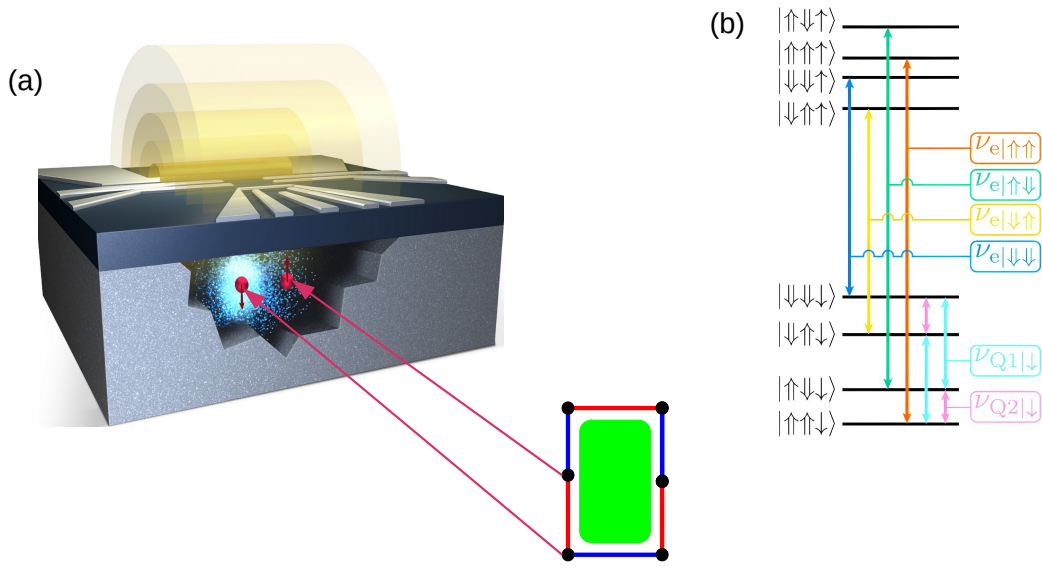


Figure 12: a) The left side of the image is an artist's representation of the 2P1e device [16], while the right side corresponds to the smallest honeycomb code cell. The two black dots in the honeycomb code represent the two phosphorus atoms that are physical qubits in the 2P1e device, shown in pink. The ancilla qubit is the electron in our system. With the 2P1e system, we are able to demonstrate the smallest parity check circuit, which is the smallest component of the Honeycomb code cell. b) NMR and ESR transitions in the eight-dimensional Hilbert space of the two-phosphorus cluster when loaded with an electron. The pink and light blue lines represent the NMR frequencies, while the remaining lines represent the ESR frequencies. Adapted from Ref. [16]

The XX -SSPC gate, shown in Fig. 8c(a), involves operations on both the electron and the nuclei, which require different time scales due to the vastly different

gyromagnetic ratios. It is no longer immediately obvious that the whole operation can be executed in a single step. In order to verify whether an XX -SSPC gate exists, we adopt a widespread quantum control optimization algorithm known as GRAPE (Gradient Ascent Pulse Engineering) [63], which can be found within QuTip [64]. One of the reasons we chose to use GRAPE is because it enables us to account for real-life experimental limitations such as the maximum and minimum control amplitudes. Another reason is that the GRAPE algorithm was originally designed for NMR pulses [63][65] and finds practical application in many experimental studies [66]. Notably, the results of the first experiment in quantum error correction in 1998 [67] were greatly improved through the utilization of the GRAPE algorithm in 2011 [68]. The GRAPE algorithm in QUTIP, is wrapped by the L-BFGS-B [69][70] optimization algorithm which takes into account second order derivatives and chooses the step size which is the change of position in the control landscape by itself. This helps the algorithm to use a smaller number of iterations. We utilized this algorithm in two distinct ways, namely modulated GRAPE and non-modulated GRAPE. The non-modulated GRAPE does not use the modulated control Hamiltonian, but it does use a control Hamiltonian with proper frequencies for both the electron and nucleus and control fields applied in two different directions (x and y). The modulated GRAPE, however, allows us to use a modulated control Hamiltonian, and we refer to this version of the algorithm as modulated GRAPE.

For the modulated GRAPE method, we took into account the $\cos(\omega t)$ term and we modulated the control Hamiltonian with $\cos(\omega t)$ for each time slot with a proper angular frequency. As a first step, we set the maximum control amplitude (the B_1 magnetic field in our case) in the range of millitesla and we ran the algorithm for 1, 10, 100, 1000 microseconds evolution time for the XX gate. The number of time slots is one of the most important parameters of the algorithm. We need to provide a fine enough resolution to observe the oscillation of the pulse. Since we are in the laboratory frame, the time interval is determined by the highest frequency in the system, which in this case is the electron Larmor frequency. In a 1.33 T magnetic field, the electron precesses at 27.97 GHz, corresponding to period of 35 ps. When the number of sampling per oscillation is taken into account, for each evolution time, the minimum time resolution is maintained at 10 picoseconds by allocating the appropriate number of time slots. To execute the algorithm with such a small time resolution, we utilized the High-Performance Computing (HPC) cluster 9. As a result, we could have the perfect gate fidelity for evolution time is in the range of

$10\mu s$.

We then attempted to find a shorter gate evolution time. In order to achieve this, we increased the control amplitude in a manner that remains experimentally feasible. We set the evolution time to 4 microseconds for the XX gate. We set upper and lower bounds to 40 mT for the control field and we used 400,000 time slots which correspond to every 10 picoseconds for a pulse. We run the algorithm for every frequency in the system and the algorithm was able to find XX parity check gates with a single pulse with an accuracy of 0.9999¶ The first 100 ns of the control amplitudes are shown in Figure 13.

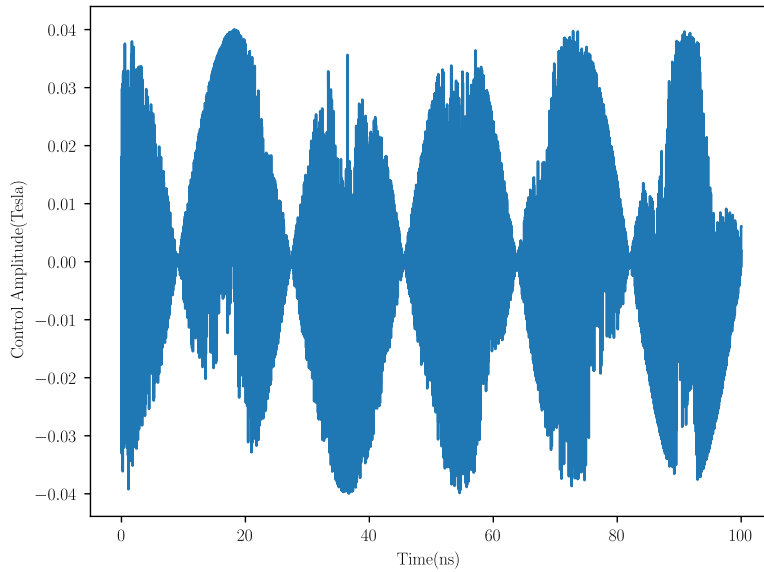


Figure 13: The first 100 ns of the optimised control pulses for the XX gate. The control amplitude represents the B_1 magnetic field applied to the spins.

To verify that the pulse found by GRAPE was physically meaningful, we then calculated its Fourier transform, shown in Figure 13.

¶ This is the theoretical fidelity and this demonstrates the feasibility of implementing this gate under the given conditions.

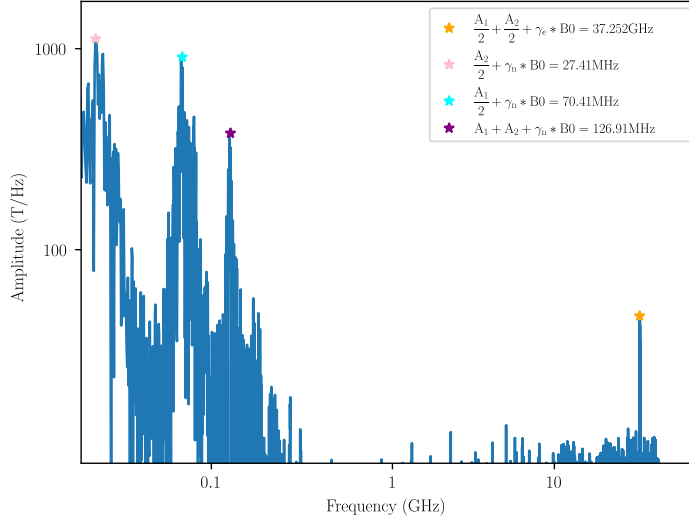


Figure 14: Fourier Transform of the GRAPE Pulse that implements the XX -SSPC gate. The peak in the spectra correspond to the natural resonance frequencies of the electron and the nuclei. The colors of stars represent the transitions, which are drawn with the same color in the Figure 12

Since the XX gate is an entangling gate formed through a combination of operations on both nuclei and electrons, we expect it to consist of control signals at the natural resonance frequencies of the electron (ESR) and the nuclei (NMR). Indeed, the frequency spectrum in Figure 13 reveals all the expected frequencies: electron spin resonance (orange marker in Fig. 13, corresponding to the orange line in Fig. 12b), and nuclear magnetic resonances (blue for nucleus 1, pink for nucleus 2). Interestingly, GRAPE also uses a stimulus at frequency $A_1 + A_2 + \gamma_n B_0$ which does not correspond to any natural resonance of the system (purple marker in Fig. 13)

We then tried to find a pulse for even shorter evolution times. The shortest evolution time that we could find a pulse for is 2 microseconds with a 0.98 fidelity with a modulated control Hamiltonian in the x direction. Note that, when we decreased the total evolution time from 4 microseconds to 2 microseconds, we also decreased the time resolution from 400,000 points to 200,000 points so that the time resolution stayed the same.

Overall, GRAPE was consistently able to find one single pulse that can implement the gate without decomposing it into one- and two-qubit gates, and

which does not require exceedingly long gate times while taking into account the experimental limitations on the maximum control amplitude.

To understand whether there are any advantages or disadvantages in terms of experimental feasibility of using the XX gate over the decomposed parity check circuit, we took a further step and attempted to implement the decomposed parity check circuit, as defined in Figure 8a, by individually implementing each one- and two-qubit gate using GRAPE. Surprisingly, while we were able to implement the Hadamard gates within a proper gate evolution time of 0.5 microseconds, the implementation of CNOT gates with high fidelity required a much longer time, around 100 microseconds. As a result, the total timing for the decomposed parity check circuit fell within the range of 100s microseconds. This analysis shows that the system under study – two nuclear spins hyperfine-coupled to an electron – is naturally suited to implement a SSPC gate, thanks to the fact that each qubit has a separate resonance frequency, and that the ancilla (the electron) has resonances that each constitute a natural rotation conditional on the state of the two nuclei.

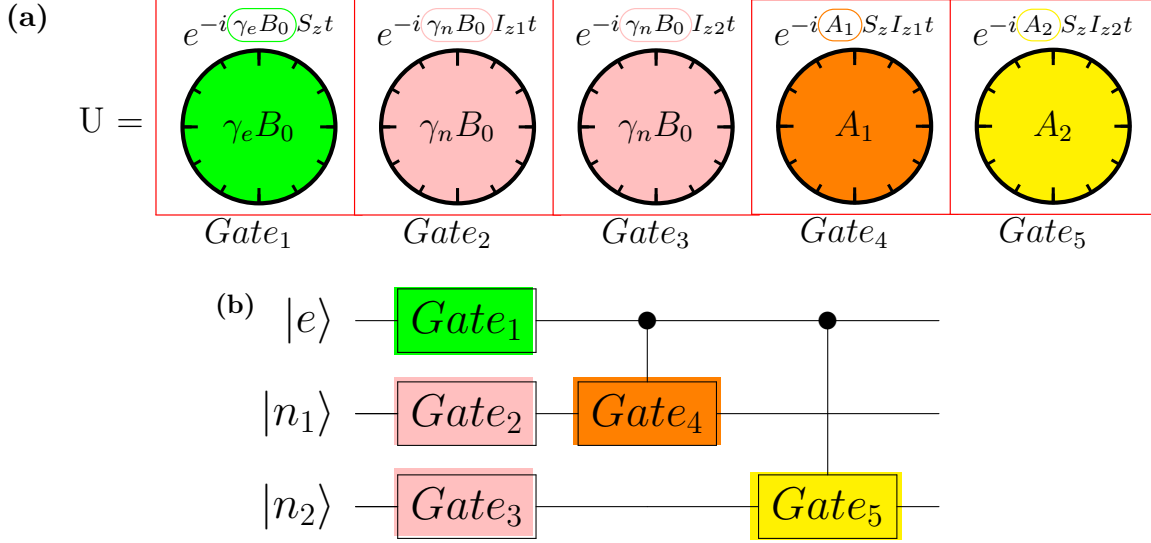


Figure 15: a) Clock dynamics of the simplified Ising drift Hamiltonian in the laboratory frame. Every term in the time evolution operator of the drift Hamiltonian can be associated with a gate with a specific ‘clock’. The colors of the clocks differentiate the times for completion of each gates. $Gate_1$ is a single qubit gate on the electron, with clock speed is $\gamma_e B_0$. $Gate_2$ and $Gate_3$ are the single qubit gates on the nuclei, with clock speed $\gamma_n B_0$. The hyperfine interactions in the drift Hamiltonian, A_1 and A_2 , are used to generate the entangling operations $Gate_4$ (between electron and nucleus 1) and $Gate_5$ (between electron and nucleus 2). b) Circuit diagram of the gates depicted in panel a). Note that these are just the gate arising from the drift Hamiltonian. The SSPC gate shown in fig. 13 requires adding the control Hamiltonian, Eq. 33.

In the next part of this work, we analytically study a modified drift Hamiltonian to gain an understanding of the appropriate timescale for the SSPC gate and the decomposed parity check circuit. In pursuit of this goal, we performed a thorough investigation of the clock dynamics associated with the drift Hamiltonian in the laboratory frame. To afford an analytical solution, we approximate the drift Hamiltonian as an Ising type modification to Equation 32. While the result of GRAPE, explicitly examines the active pulsing required to realize the unitary for the SSPC gate without loss of generality, here we analytically examine the passive drift Hamiltonian for the Ising Hamiltonian in Equation 34.

$$H = -\gamma_e B_0 S_z - \gamma_n B_0 I_{z1} - \gamma_n B_0 I_{z2} + A_1 S_z I_{z1} + A_2 S_z I_{z2} \quad (34)$$

The time evolution operator, $U = e^{iHt}$, can be expanded as

$$U = \underbrace{e^{-i(\gamma_e B_0)S_Z t}}_{Gate_1} \underbrace{e^{-i(\gamma_n B_0)I_{z1} t}}_{Gate_2} \underbrace{e^{-i(\gamma_n B_0)I_{z2} t}}_{Gate_3} \underbrace{e^{i(A_1)S_z I_{z1} t}}_{Gate_4} \underbrace{e^{i(A_2)S_z I_{z2} t}}_{Gate_5} \quad (35)$$

Every exponential term in Equation 35, which are the free evolution times of the drift Hamiltonian, will generate a gate and every gate will have its own clock. These clocks correspond to the time taken for the desired gates. $Gate_1$, $Gate_2$, $Gate_3$, $Gate_4$ and $Gate_5$ are the natural gates which can be obtain from the evolution of the drift Hamiltonian. However, if we want to create specific gates, such as a CZ gate between an electron and the first nucleus using the hyperfine interaction denoted as A_1 , in other words, if we want $Gate_4$ to function as a CZ gate, then we need to have the control Hamiltonian and pulse the system. In this part of the study, our focus is on understanding the approximate timescale for the SSPC gate and the decomposed parity check circuit that were derived by using GRAPE. When considering the control Hamiltonian, the time required for the SSPC gate and the decomposed parity check circuit will change. However, the proportion of the timescales between the SSPC gate and the decomposed parity check circuit will be comparable for analytical analysis and the numerical analysis. In this part of the study, since we are not using the control Hamiltonian, we do not refer to the gates as CZ gate or ZZ gate. Instead, we refer to them as CZ-like gate and ZZ-like gate. Now, if we want to implement a decomposed ZZ parity check circuit which is shown in Figure 9a, we need to implement CZ-like dynamics, since the ZZ parity check circuit can be implemented either by using the CZ gate with Hadamard gates or directly with two CNOT gates. However, if we want to implement an entangling gate between the electron and the first nucleus, we need to use the hyperfine strength A_1 . Due to the hyperfine strength A_2 , the system will be disturbed. Because, the hyperfine interaction is always on; we can't turn it off, change it, or tune it. It is one of the key properties of the system and we can't manipulate it. This is why we need to find a time that allows us to perform an entangling gate between the electron and the first nucleus and the identity between the electron and the second nucleus so that the second hyperfine interaction does not disturb the system. To find such a time, we need to consider the clock dynamics of the drift Hamiltonian. The first entangling gate will be between the electron and the first nucleus. A π rotation around the Bloch sphere will be a CZ rotation since $e^{i\pi} = -1$. The time for $Gate_4$ to function as a CZ-like gate will

be $\pi/95$ MHz ≈ 33.06 nanoseconds. However, it is also imperative to ensure that the system remains unaffected by the hyperfine interaction between the electron and the second nuclei. Therefore, it is crucial that $Gate_5$ should function as identity operation. This means that while $Gate_4$ makes a π rotation around the bloch sphere, $Gate_5$ should make a 2π rotation. The time taken for $Gate_5$ to function as identity is $2\pi/9$ MHz ≈ 698.13 nanoseconds. Now, for finding an appropriated time, we need to solve the Equation 36:

$$\begin{aligned} ((a * t_{Gate4}) - (b * t_{Gate5}))^2 &\leq error^2, a > 0, b > 0, \\ \text{where } a \text{ is an odd integer and } b \text{ is an integer} \end{aligned} \quad (36)$$

Here, the error is defined as 0.01 so that $error^2 = 0.0001$ which is less than a square of radian correspondence of 1 degree. It turns out that, the possible fastest time occurs when we round the time taken for the single π rotation for $Gate_4$ to be 33.1 ns and the time taken for the single 2π rotation for $Gate_5$ to be 698.1 ns. In this situation, the evolution of $Gate_4$ should at least make $a = 6981$ π rotations while the evolution of $Gate_5$ should at least make $b = 331$ 2π rotations so that we can have a perfect CZ-like gate. The total time for a perfect CZ-like gate between the electron and the first nuclei is $33.1 * 6981 = 231.07 \mu s$

Now, if we want to make a perfect CZ-like gate between the electron and the second nucleus, one π rotation for $Gate_5$ to function as a CZ-like is equal to $\pi/9$ MHz ≈ 349.06 nanoseconds and the time for one 2π rotation for $Gate_4$ to function as identity is equal to ≈ 66.13 nanoseconds. If we solve the Equation 37,

$$\begin{aligned} ((a * t_{Gate5}) - (b * t_{Gate4}))^2 &\leq error^2, a > 0, b > 0, \\ \text{where } a \text{ is an odd integer and } b \text{ is an integer} \end{aligned} \quad (37)$$

the fastest possible time will occur when we take a single π rotation time for $Gate_5$ as 349.06 ns and single 2π rotation time for $Gate_4$ as 66.13 ns. In this case, $a = 887$ is the number of π rotations for the evolution of $Gate_5$. Correspondingly, the total time for a clear CZ-like gate for the electron and the second nucleus is equal to $349.06 * 887 = 309.06 \mu s$. As a result, if we want to implement the circuit which is defined in Figure 9a, the simplified Hamiltonian can naturally achieve that in a range of hundreds μs . In the second part of this analytical calculation, we will analyze the drift Hamiltonian for the ZZ-like gate. For implementing such a gate, both the $Gate_4$ and the $Gate_5$ should function as CZ gates so they should make a

π rotation. For $Gate_4$ to function as CZ-like, the time for one single π rotation is $\pi/95$ MHz = 33.06 nanoseconds and for $Gate_5$, the time for one single π rotation is $\pi/9$ MHz = 349.06 nanoseconds. To see if our drift Hamiltonian can have a suitable time for such a gate, we need to solve Equation 38.

$$\begin{aligned} ((a * t_{Gate4}) - (b * t_{Gate5}))^2 &\leq error^2, a > 0, b > 0, \\ &\text{where both a and b are an odd integer} \end{aligned} \quad (38)$$

It turns out that even without rounding the numbers, it is found that $a = 1805$ and $b = 171$ which means that the total time for the desired unitary is $\cong 60 \mu s$. As a result, implementing two separated CZ-like dynamics requires $\approx 540.13 \mu s$ in total whereas implementing a ZZ-like dynamics requires $\approx 60 \mu s$ which is 9 times faster than implementing a traditional parity check circuit. This explanation clarifies that why the GRAPE algorithm discovered the SSPC gate approximately 10 times faster than the decomposed parity check circuit. This is because the SSPC gate does not suffer from imbalanced hyperfine interaction, whereas the isolated entangling gate does. The codes concerning this section, encompassing both the xx gate and the decomposed parity check gate, can be found in [71][72].

7. Conclusions

In this theory work, we developed a workflow which calculates the perfection rate of the whole parity check with given experimental data. We numerically showed how errors are accumulating and causing a decrease of the perfection rate of the parity check circuit with current sources (with single and two qubit gate and M_{pp1}) from the experimental GST matrices. Our findings indicate that relying solely on the fidelity of single and two qubit gate operations is inadequate in assessing the effectiveness of constructing the fundamental elements of quantum error correction, specifically the parity check circuits. Then, we introduced new full unitaries which allow us to make parity check measurement in one step. We call these unitaries single step parity check gate set. We modified the universal gate set such that the new unitaries are the most natural gate set for QEC. We compared the traditional parity check gate (single and two qubits gates) and the SSPC gate for an XX parity check scenario in the presence of noise.

We provided an experimentally realizable example based on spin qubits in silicon, and used the GRAPE algorithm to find a single pulse capable of implementing

the single-step parity check gate within experimental limitations. Furthermore, we implemented the decomposed parity check circuit using GRAPE. We found that SSPC gate is naturally suited for this system, and outperforms a decomposed gate.

Many have asked what the “killer-app” is for a large-scale, error-corrected quantum computer, this is error-correction. The vast majority of the computation occurring in a large-scale machine is dedicated to correcting its own errors. As such, fundamental gate sets used at the physical level should be targeted at this application. We have introduced a complete workflow that allows experimentalists to characterise more complex gate sets and connect outputs of characterisation experiments to commonly used models used in QEC analysis. This allows hardware efforts to potentially redesign and test fundamental gate libraries, increasing performance, and accelerating the realisation of fault-tolerant, error-corrected quantum computers.

8. Data availability statement

The algorithm for finding the perfection rate and the errors in the context of quantum error correction from experimental data can be found in [59].

All the code regarding the GRAPE algorithm can be found in [71] and in [72]

9. Acknowledgments

The work was funded by the Australian Research Council (CE170100012). G.Ü acknowledges support from the Sydney Quantum Academy. This research was undertaken with the assistance of resources and services from the National Computational Infrastructure (NCI), which is supported by the Australian Government. SJD was supported with funding from the Defense Advanced Research Projects Agency [under the Quantum Benchmarking (QB) program under award no. HR00112230007 and HR001121S0026 contracts]. The views, opinions and/or findings expressed are those of the authors and should not be interpreted as representing the official views or policies of the Department of Defense or the U.S. Government. We thank S. Asaad, M. Mađzik and R. Savytsky for sharing GST experimental results and useful discussions. We thank B.C. Sanders for discussions on quantum control and optimal pulse methods, and A. Pitchford for support on the GRAPE algorithm.

Appendices

A-1. Calculating the Final Density Matrix in terms of Having Certain Errors

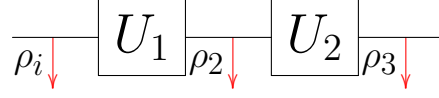


Figure A.1: One qubit circuit example which will be used to calculate effective errors in the context of QEC. At the beginning, the circuit will have the ρ_i , after applying U_1 gate, the density matrix will become ρ_2 and the final density matrix will be ρ_3 after applying U_3 .

Let's start with writing ρ_2

$$\rho_2 = p_{i1}IU_1\rho_iU_1^\dagger I + p_{x1}XU_1\rho_iU_1^\dagger X + p_{y1}YU_1\rho_iU_1^\dagger Y + p_{z1}ZU_1\rho_iU_1^\dagger Z \quad (\text{A.1})$$

where p_{i1} is the perfection rate of U_1 gate. $p_x, p_y,$ and p_z respectively represent the probabilities of having $X, Y,$ and Z errors in the channel after applying the unitary U_1 . The system now in ρ_2 . Then we apply U_2 gates and the system becomes ρ_3 .

$$\rho_3 = p_{i2}IU_2\rho_2U_2^\dagger I + p_{x2}XU_2\rho_2U_2^\dagger X + p_{y2}YU_2\rho_2U_2^\dagger Y + p_{z2}ZU_2\rho_2U_2^\dagger Z \quad (\text{A.2})$$

where p_{i2} is the perfection of U_2 gate which. p_{x2}, p_{y2} and p_{z2} respectively represent the probabilities of having $X, Y,$ and Z errors in the channel after applying the unitary U_2 . If we put Equation A.1 in Equation A.2, then we will have:

$$\begin{aligned} \rho_3 = & \overline{[p_{i2}]}IU_2\overline{[p_{i1}]}IU_1\rho_iU_1^\dagger I + p_{x1}XU_1\rho_iU_1^\dagger X + p_{y1}YU_1\rho_iU_1^\dagger Y + p_{z1}ZU_1\rho_iU_1^\dagger Z]U_2^\dagger I + \\ & \overline{[p_{x2}]}XU_2\overline{[p_{i1}]}IU_1\rho_iU_1^\dagger I + \overline{[p_{x1}]}XU_1\rho_iU_1^\dagger X + p_{y1}YU_1\rho_iU_1^\dagger Y + p_{z1}ZU_1\rho_iU_1^\dagger Z]U_2^\dagger X + \\ & \overline{[p_{y2}]}YU_2\overline{[p_{i1}]}IU_1\rho_iU_1^\dagger I + p_{x1}XU_1\rho_iU_1^\dagger X + \overline{[p_{y1}]}YU_1\rho_iU_1^\dagger Y + p_{z1}ZU_1\rho_iU_1^\dagger Z]U_2^\dagger Y + \\ & \overline{[p_{z2}]}ZU_2\overline{[p_{i1}]}IU_1\rho_iU_1^\dagger I + p_{x1}XU_1\rho_iU_1^\dagger X + p_{y1}YU_1\rho_iU_1^\dagger Y + \overline{[p_{z1}]}ZU_1\rho_iU_1^\dagger Z]U_2^\dagger Z \end{aligned} \quad (\text{A.3})$$

Now, the coefficients are inside the dashed lines gives us to total perfection of the circuit after applying operations. As a result we get Equation A.4:

$$P_I = p_{i2}p_{i1} + p_{x2}p_{x1} + p_{y2}p_{y1} + p_{z2}p_{z1} \quad (\text{A.4})$$

where P_I is the perfection rate of the widget after applying all the unitaries in the quantum circuit. For the accumulated errors, for instance the accumulated x errors,

we will have the equation A.5:

$$P_X = p_{i2}p_{x1} + p_{x2}p_{i1} + p_{y2}p_{z1} + p_{z2}p_{y1} \quad (\text{A.5})$$

If we had only one step, we would have ρ_2 exclusively. In that case, P_I would be equal to p_{i1} , and the X error would be represented by $p_x = p_{x1}$. However, as the circuit depth increases, the occurrences of X, Y, and Z errors also increase, leading to a decrease in the fidelity P_I . In Equation A.4, it is important to note that $P_I < p_{i1}$ since errors accumulate within the circuit.

A-2. Tutorial

Here, we will demonstrate the complete process for a single qubit. We take the circuit in Figure A.2 as an example:

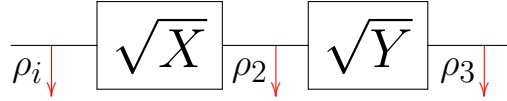


Figure A.2: One qubit circuit example which will be used to calculate effective errors in the context of QEC. At the beginning, the circuit will have the ρ_i , after applying \sqrt{X} gate, the density matrix will become ρ_2 and the final density matrix will be ρ_3 after applying \sqrt{Y} .

We take the data from [73]. The average fidelity of the single qubit operation is 98.4%. The experimental GST matrix for \sqrt{X} gate is A.6.

$$\sqrt{X}_{GST-exp} = \begin{pmatrix} 1 & 0 & 0 & 0 \\ 8.86E-04 & 0.9864307 & 0.0196069 & 0.0404753 \\ 0.0143302 & 0.0103946 & 0.0185571 & -0.9569604 \\ -0.0278189 & -0.0312292 & 0.9486933 & 0.0084777 \end{pmatrix} \quad (\text{A.6})$$

The ideal GST matrix for \sqrt{X} gate is A.7.

$$\sqrt{X}_{GST-ideal} = \begin{pmatrix} 1 & 0 & 0 & 0 \\ 0 & 1 & 0 & 0 \\ 0 & 0 & 0 & -1 \\ 0 & 0 & 1 & 0 \end{pmatrix} \quad (\text{A.7})$$

Now the complete GST matrix for \sqrt{X} gate will be A.8

$$\sqrt{X}_{GST} = \sqrt{X}_{GST-ideal}^\dagger \times \sqrt{X}_{GST-exp} \quad (\text{A.8})$$

$$\sqrt{X}_{GST} = \begin{pmatrix} 1 & 0 & 0 & 0 \\ 8.860000e-04 & 9.864307e-01 & 1.960690e-02 & 4.047530e-02 \\ -2.781890e-02 & -3.122920e-02 & 9.486933e-01 & 8.477700e-03 \\ -1.433020e-02 & -1.039460e-02 & -1.855710e-02 & 9.569604e-01 \end{pmatrix} \quad (\text{A.9})$$

We then specify the matrix type in Equation A.9 as PTM [47] [46][57] and then, we find the Kraus Operators for \sqrt{X} gate:

$$A_{k1} = \begin{pmatrix} -9.82824463e-01 - 1.52153329e-17j & 1.24054742e-02 - 1.43214994e-02j \\ -1.33256506e-02 + 5.94368403e-05j & -9.89833481e-01 + 2.61770785e-02j \end{pmatrix} \quad (\text{A.10})$$

$$A_{k2} = \begin{pmatrix} 7.26849880e-02 + 2.13046306e-16j & 9.65945754e-02 - 6.73574945e-02j \\ 1.05026446e-01 - 1.32068469e-01j & -7.12956263e-02 + 4.21055119e-03j \end{pmatrix} \quad (\text{A.11})$$

$$A_{k3} = \begin{pmatrix} 9.31488789e-03 + 4.15059375e-16j & -2.72802393e-03 + 1.08353965e-02j \\ -5.36428664e-03 - 1.59739616e-03j & -9.35810153e-03 + 3.65639053e-04j \end{pmatrix} \quad (\text{A.12})$$

$$A_{k4} = \begin{pmatrix} 1.14031245e-03 + 1.92254246e-12j & -4.04058392e-04 - 1.77301906e-03j \\ -3.19532408e-06 + 1.83340351e-03j & -1.11211291e-03 - 2.33383741e-05j \end{pmatrix} \quad (\text{A.13})$$

To verify whether we have identified the correct Kraus operators, we need to apply Equation 18. After applying Equation 18, if we obtain the identity matrix, it indicates that the Kraus operators we have determined are correct. The subsequent step involves expanding each Kraus operator in terms of Pauli matrices. Therefore, we will have the following expressions:

$$\begin{aligned} A_{k1} = & (-0.98633 + 0.01309j)I + \\ & (-0.00046 - 0.00713j)X + \\ & (0.00719 + 0.01287j)Y + \\ & (0.0035 - 0.01309j)Z \end{aligned} \quad (\text{A.14})$$

$$\begin{aligned}
A_{k2} = & (0.00069 + 0.00211j)I + \\
& (0.10081 - 0.09971j)X + \\
& (-0.03236 - 0.00422j)Y + \\
& (0.07199 - 0.00211j)Z
\end{aligned} \tag{A.15}$$

$$\begin{aligned}
A_{k3} = & -2e - 05 + 0.00018j)I + \\
& (-0.00405 + 0.00462j)X + \\
& (-0.00622 + 0.00132j)Y + \\
& (0.00934 - 0.00018j)Z
\end{aligned} \tag{A.16}$$

$$\begin{aligned}
A_{k4} = & (1e - 05 - 1e - 05j)I + \\
& (-0.0002 + 3e - 05j)X + \\
& (0.0018 - 0.0002j)Y + \\
& (0.00113 + 1e - 05j)Z
\end{aligned} \tag{A.17}$$

To obtain the total final density matrix for the \sqrt{X} gate, we apply Equation 22. We square the absolute value of each coefficient and then sum the coefficients based on their respective groups. As a result, we obtain Equation A.18.

$$\begin{aligned}
\rho_2 = \rho_{\sqrt{X}} = & (0.973023 + 0j)I + \\
& (0.020194 + 0j)X \rho_i X + \\
& (0.001325 + 0j)Y \rho_i Y + \\
& (0.005458 + 0j)Z \rho_i Z
\end{aligned} \tag{A.18}$$

As seen from Equation A.18, the value of p_i is 0.973, which is not equal to the average fidelity of the 1Q gate operation, which is 98.4%. Next, we perform the same process for the \sqrt{Y} gate:

$$\sqrt{Y}_{GST-exp} = \begin{pmatrix} 1 & 0 & 0 & 0 \\ -0.00995 & 0.0317816 & 0.0360635 & 0.9617441 \\ -0.0015329 & 0.0423713 & 0.9805663 & -0.0148585 \\ -0.0090296 & -0.9691875 & 0.0085467 & 0.0140323 \end{pmatrix} \tag{A.19}$$

The ideal GST matrix for \sqrt{Y} gate is A.20.

$$\sqrt{Y}_{GST-ideal} = \begin{pmatrix} 1 & 0 & 0 & 0 \\ 0 & 0 & 0 & 1 \\ 0 & 0 & 1 & 0 \\ 0 & -1 & 0 & 0 \end{pmatrix} \quad (\text{A.20})$$

The final density matrix for \sqrt{Y} gate is found as Equation A.21.

$$\begin{aligned} \rho_3 = \rho_{\sqrt{Y}} = & (0.97787447)I + \\ & (0.00671927 + 0j)X \rho_2 X \\ & (0.01240868 + 0j)Y \rho_2 Y + \\ & (0.00299758 + 0j)Z \rho_2 Z \end{aligned} \quad (\text{A.21})$$

As it seen from Equation A.21, ρ_3 has ρ_2 . To calculate final coefficients of ρ_3 , we put the Equation A.18 in Equation A.21 as it shown in A.3. Then we calculate the P_I coefficient by the Equation A.4.

$$\begin{aligned} P_I = & (0.97787447) * (0.973023) + \\ & (0.00671927) * (0.020194) + \\ & (0.01240868) * (0.001325) + \\ & (0.00299758) * (0.005458) \end{aligned} \quad (\text{A.22})$$

$$P_I = 0.9517 \quad (\text{A.23})$$

As a result Figure A.2 becomes Figure A.3:

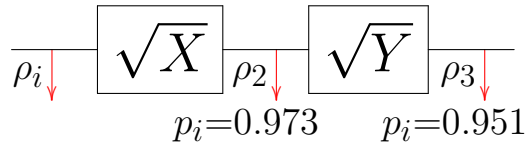


Figure A.3: The figure shows how accumulated errors decrease the perfection rate of the circuit which is P_I . Density matrix in terms of having certain errors in QEC is calculated. After applying \sqrt{X} gate, the value of perfection was found as 0.973. After applying \sqrt{Y} , the perfection value decreased 0.951

A-.3. Density Matrix in Terms of QEC for 2 qubit

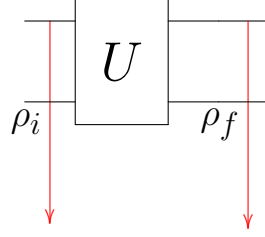


Figure A.4: Two Qubits Circuit example with o which will be used to calculate effective errors in the context of QEC.

$$\begin{aligned}
\rho_f = & p_{ii}I \otimes IU\rho_iU^\dagger(I \otimes I)^\dagger + p_{xx}X \otimes XU\rho_iU^\dagger(X \otimes X)^\dagger + \\
& p_{yy}Y \otimes YU\rho_iU^\dagger(Y \otimes Y)^\dagger + p_{zz}Z \otimes ZU\rho_iU^\dagger(Z \otimes Z)^\dagger + \\
& p_{ix}I \otimes XU\rho_iU^\dagger(I \otimes X)^\dagger + p_{iy}I \otimes YU\rho_iU^\dagger(I \otimes Y)^\dagger + \\
& p_{iz}Z \otimes ZU\rho_iU^\dagger(I \otimes Z)^\dagger + p_{xi}X \otimes IU\rho_iU^\dagger(X \otimes I)^\dagger + \\
& p_{xy}X \otimes YU\rho_iU^\dagger(X \otimes Y)^\dagger + p_{xz}X \otimes ZU\rho_iU^\dagger(X \otimes Z)^\dagger + \\
& p_{yi}Y \otimes IU\rho_iU^\dagger(Y \otimes I)^\dagger + p_{yx}Y \otimes XU\rho_iU^\dagger(Y \otimes X)^\dagger + \\
& p_{yz}Y \otimes ZU\rho_iU^\dagger(Y \otimes Z)^\dagger + p_{zi}Z \otimes IU\rho_iU^\dagger(Z \otimes I)^\dagger + \\
& p_{zx}Z \otimes XU\rho_iU^\dagger(Z \otimes X)^\dagger + p_{zy}Z \otimes YU\rho_iU^\dagger(Z \otimes Y)^\dagger
\end{aligned} \tag{A.24}$$

A-.4. Density Matrix in Terms of QEC for 3 qubit

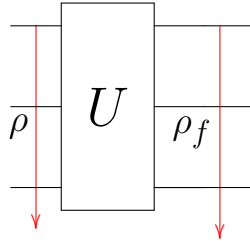


Figure A.5: Three Qubits Circuit example with o which will be used to calculate effective errors in the context of QEC.

$$\begin{aligned}
\rho_f = & p_{iii}I \otimes I \otimes IU\rho U^\dagger(I \otimes I \otimes I)^\dagger + p_{iix}I \otimes I \otimes XU\rho U^\dagger(I \otimes I \otimes X)^\dagger + \\
& p_{iiy}I \otimes I \otimes YU\rho U^\dagger(I \otimes I \otimes Y)^\dagger + p_{iiz}I \otimes I \otimes ZU\rho U^\dagger(I \otimes I \otimes Z)^\dagger + \\
& p_{ixi}I \otimes X \otimes IU\rho U^\dagger(I \otimes X \otimes I)^\dagger + p_{ixx}I \otimes X \otimes XU\rho U^\dagger(I \otimes X \otimes X)^\dagger + \\
& p_{ixy}I \otimes X \otimes YU\rho U^\dagger(I \otimes X \otimes Y)^\dagger + p_{ixz}I \otimes X \otimes ZU\rho U^\dagger(I \otimes X \otimes Z)^\dagger + \\
& p_{iyi}I \otimes Y \otimes IU\rho U^\dagger(I \otimes Y \otimes I)^\dagger + p_{iyx}I \otimes Y \otimes XU\rho U^\dagger(I \otimes Y \otimes X)^\dagger + \\
& p_{iyy}I \otimes Y \otimes YU\rho U^\dagger(I \otimes Y \otimes Y)^\dagger + p_{iyz}I \otimes Y \otimes ZU\rho U^\dagger(Y \otimes Z)^\dagger + \\
& p_{izi}I \otimes Z \otimes IU\rho U^\dagger(I \otimes Z \otimes I)^\dagger + p_{izx}Z \otimes XU\rho U^\dagger(Z \otimes X)^\dagger + \\
& p_{izy}I \otimes Z \otimes YU\rho U^\dagger(I \otimes Z \otimes Y)^\dagger + p_{izz}I \otimes Z \otimes ZU\rho U^\dagger(I \otimes Z \otimes Z)^\dagger + \\
& p_{xii}X \otimes I \otimes IU\rho U^\dagger(X \otimes I \otimes I)^\dagger + p_{xix}X \otimes I \otimes XU\rho U^\dagger(X \otimes I \otimes X)^\dagger + \\
& p_{xiy}X \otimes I \otimes YU\rho U^\dagger(X \otimes I \otimes Y)^\dagger + p_{xiz}X \otimes I \otimes ZU\rho U^\dagger(X \otimes I \otimes Z)^\dagger + \\
& p_{xxi}X \otimes X \otimes IU\rho U^\dagger(X \otimes X \otimes I)^\dagger + p_{xxx}X \otimes X \otimes XU\rho U^\dagger(X \otimes X \otimes X)^\dagger + \\
& p_{xxy}X \otimes X \otimes YU\rho U^\dagger(X \otimes X \otimes Y)^\dagger + p_{xxz}X \otimes X \otimes ZU\rho U^\dagger(X \otimes X \otimes Z)^\dagger + \\
& p_{xyi}X \otimes Y \otimes IU\rho U^\dagger(X \otimes Y \otimes I)^\dagger + p_{xyx}X \otimes Y \otimes XU\rho U^\dagger(X \otimes Y \otimes X)^\dagger + \\
& p_{xyy}X \otimes Y \otimes Y\rho(X \otimes Y \otimes Y)^\dagger + p_{xyz}X \otimes Y \otimes ZU\rho U^\dagger(X \otimes Y \otimes Z)^\dagger + \\
& p_{xzi}X \otimes Z \otimes IU\rho U^\dagger(X \otimes Z \otimes I)^\dagger + p_{zxz}X \otimes Z \otimes XU\rho U^\dagger(X \otimes Z \otimes X)^\dagger + \\
& p_{xzy}X \otimes Z \otimes YU\rho U^\dagger(X \otimes Z \otimes Y)^\dagger + p_{xzz}X \otimes Z \otimes ZU\rho U^\dagger(X \otimes Z \otimes Z)^\dagger + \\
& p_{yii}Y \otimes I \otimes IU\rho U^\dagger(Y \otimes I \otimes I)^\dagger + p_{yix}Y \otimes I \otimes XU\rho U^\dagger(Y \otimes I \otimes X)^\dagger + \\
& p_{yiy}Y \otimes I \otimes YU\rho U^\dagger(Y \otimes I \otimes Y)^\dagger + p_{yiz}Y \otimes I \otimes ZU\rho U^\dagger(Y \otimes I \otimes Z)^\dagger + \\
& p_{yxi}Y \otimes X \otimes IU\rho U^\dagger(Y \otimes X \otimes I)^\dagger + p_{yxx}Y \otimes X \otimes XU\rho U^\dagger(Y \otimes X \otimes X)^\dagger + \\
& p_{yxy}Y \otimes X \otimes YU\rho U^\dagger(Y \otimes X \otimes Y)^\dagger + p_{yxz}Y \otimes X \otimes ZU\rho U^\dagger(Y \otimes X \otimes Z)^\dagger + \\
& p_{yyi}Y \otimes Y \otimes IU\rho U^\dagger(Y \otimes Y \otimes I)^\dagger + p_{yyx}Y \otimes Y \otimes XU\rho U^\dagger(Y \otimes Y \otimes X)^\dagger + \\
& p_{yyy}Y \otimes Y \otimes YU\rho U^\dagger(Y \otimes Y \otimes Y)^\dagger + p_{yyz}Y \otimes Y \otimes ZU\rho U^\dagger(Y \otimes Y \otimes Z)^\dagger + \\
& p_{yzi}Y \otimes Z \otimes IU\rho U^\dagger(Y \otimes Z \otimes I)^\dagger + p_{yzx}Y \otimes Z \otimes XU\rho U^\dagger(Y \otimes Z \otimes X)^\dagger + \\
& p_{yzy}Y \otimes Z \otimes YU\rho U^\dagger(Y \otimes Z \otimes Y)^\dagger + p_{yzz}Y \otimes Z \otimes ZU\rho U^\dagger(Y \otimes Z \otimes Z)^\dagger + \\
& p_{zii}Z \otimes I \otimes IU\rho U^\dagger(Z \otimes I \otimes I)^\dagger + p_{zix}Z \otimes I \otimes XU\rho U^\dagger(Z \otimes I \otimes X)^\dagger + \\
& p_{ziy}Z \otimes I \otimes YU\rho U^\dagger(Z \otimes I \otimes Y)^\dagger + p_{ziz}Z \otimes I \otimes ZU\rho U^\dagger(Z \otimes I \otimes Z)^\dagger + \\
& p_{zxi}Z \otimes X \otimes IU\rho U^\dagger(Z \otimes X \otimes I)^\dagger + p_{zxx}Z \otimes X \otimes XU\rho U^\dagger(Z \otimes X \otimes X)^\dagger + \\
& p_{zxy}Z \otimes X \otimes YU\rho U^\dagger(Z \otimes X \otimes Y)^\dagger + p_{zxz}Z \otimes X \otimes ZU\rho U^\dagger(Z \otimes X \otimes Z)^\dagger + \\
& p_{zyi}Z \otimes Y \otimes IU\rho U^\dagger(Z \otimes Y \otimes I)^\dagger + p_{zyx}Z \otimes Y \otimes XU\rho U^\dagger(Z \otimes Y \otimes X)^\dagger + \\
& p_{zyy}Z \otimes Y \otimes YU\rho U^\dagger(Z \otimes Y \otimes Y)^\dagger + p_{zyz}Z \otimes Y \otimes ZU\rho U^\dagger(Z \otimes Y \otimes Z)^\dagger + \\
& p_{zzi}Z \otimes Z \otimes IU\rho U^\dagger(Z \otimes Z \otimes I)^\dagger + p_{zzx}Z \otimes Z \otimes XU\rho U^\dagger(Z \otimes Z \otimes X)^\dagger + \\
& p_{zzy}Z \otimes Z \otimes YU\rho U^\dagger(Z \otimes Z \otimes Y)^\dagger + p_{zzz}Z \otimes Z \otimes ZU\rho U^\dagger(Z \otimes Z \otimes Z)^\dagger +
\end{aligned} \tag{A.25}$$

A-.5. Coefficients for Dominated Term from 64^6

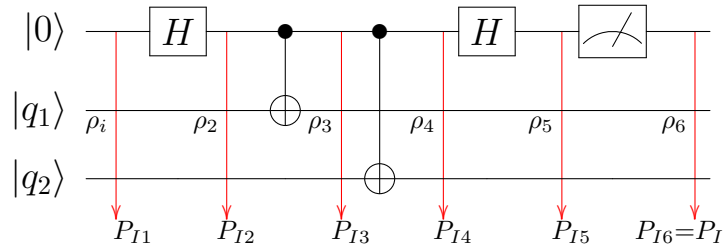


Figure A.6: analysis of XX parity check in terms of QEC. The circuit depth is 6 and we have 6 steps to calculate the widget. We first start with ρ_i . Each step that we apply the gates, the value of having no error in the channel which is P_I decrease since the errors accumulate to the next step of the circuit

$$\begin{aligned}
(P_I) = & (p_{5iii})(p_{4iii})(p_{3iii})(p_{2iii})(p_{1iii}) + p_{5iix}p_{4iix}p_{3iix}p_{2iix}p_{iix} + \\
& p_{5iyy}p_{4iyy}p_{3iyy}p_{2iyy}p_{iyy} + p_{5iiz}p_{4iiz}p_{3iiz}p_{2iiz}p_{iiz} + \\
& p_{5ixi}p_{4ixi}p_{3ixi}p_{2ixi}p_{ixi} + p_{5ixx}p_{4ixx}p_{3ixx}p_{2ixx}p_{ixx} + \\
& p_{5ixy}p_{4ixy}p_{3ixy}p_{2ixy}p_{ixy} + p_{5ixz}p_{4ixz}p_{3ixz}p_{2ixz}p_{ixz} + \\
& p_{5iyy}p_{4iyy}p_{3iyy}p_{2iyy}p_{iyy} + p_{5iyx}p_{4iyx}p_{3iyx}p_{2iyx}p_{iyx} + \\
& p_{5iyy}p_{4iyy}p_{3iyy}p_{2iyy}p_{iyy} + p_{5iyz}p_{4iyz}p_{3iyz}p_{2iyz}p_{iyz} + \\
& p_{5iyz}p_{4iyz}p_{3iyz}p_{2iyz}p_{iyz} + p_{5izi}p_{4izi}p_{3izi}p_{2izi}p_{izi} + \\
& p_{5izx}p_{4izx}p_{3izx}p_{2izx}p_{izx} + p_{5izy}p_{4izy}p_{3izy}p_{2izy}p_{izy} + \\
& p_{5izy}p_{4izy}p_{3izy}p_{2izy}p_{izy} + p_{5izz}p_{4izz}p_{3izz}p_{2izz}p_{izz} + \\
& p_{5xii}p_{4xii}p_{3xii}p_{2xii}p_{xii} + p_{5xix}p_{4xix}p_{3xix}p_{2xix}p_{xix} + \\
& p_{5xii}p_{4xii}p_{3xii}p_{2xii}p_{xii} + p_{5xix}p_{4xix}p_{3xix}p_{2xix}p_{xix} + \\
& p_{5xix}p_{4xix}p_{3xix}p_{2xix}p_{xix} + p_{5xxx}p_{4xxx}p_{3xxx}p_{2xxx}p_{xxx} + \\
& p_{5xxy}p_{4xxy}p_{3xxy}p_{2xxy}p_{xxy} + p_{5xxz}p_{4xxz}p_{3xxz}p_{2xxz}p_{xxz} + \\
& p_{5xxz}p_{4xxz}p_{3xxz}p_{2xxz}p_{xxz} + p_{5xyi}p_{4xyi}p_{3xyi}p_{2xyi}p_{xyi} + \\
& p_{5xyx}p_{4xyx}p_{3xyx}p_{2xyx}p_{xyx} + p_{5xzi}p_{4xzi}p_{3xzi}p_{2xzi}p_{xzi} + \\
& p_{5xzx}p_{4xzx}p_{3xzx}p_{2xzx}p_{xzx} + p_{5xzy}p_{4xzy}p_{3xzy}p_{2xzy}p_{xzy} + \\
& p_{5xzz}p_{4xzz}p_{3xzz}p_{2xzz}p_{xzz} + p_{5yii}p_{4yii}p_{3yii}p_{2yii}p_{yii} + \\
& p_{5yix}p_{4yix}p_{3yix}p_{2yix}p_{yix} + p_{5yiy}p_{4yiy}p_{3yiy}p_{2yiy}p_{yiy} + \\
& p_{5yiz}p_{4yiz}p_{3yiz}p_{2yiz}p_{yiz} + p_{5yxi}p_{4yxi}p_{3yxi}p_{2yxi}p_{yxi} + \\
& p_{5yxx}p_{4yxx}p_{3yxx}p_{2yxx}p_{yxx} + p_{5yxy}p_{4yxy}p_{3yxy}p_{2yxy}p_{yxy} + \\
& p_{5yxz}p_{4yxz}p_{3yxz}p_{2yxz}p_{yxz} + p_{5yyi}p_{4yyi}p_{3yyi}p_{2yyi}p_{yyi} + \\
& p_{5yyx}p_{4yyx}p_{3yyx}p_{2yyx}p_{yyx} + p_{5yyy}p_{4yyy}p_{3yyy}p_{2yyy}p_{yyy} + \\
& p_{5yyz}p_{4yyz}p_{3yyz}p_{2yyz}p_{yyz} + p_{5yzi}p_{4yzi}p_{3yzi}p_{2yzi}p_{yzi} + \\
& p_{5yzx}p_{4yzx}p_{3yzx}p_{2yzx}p_{yzx} + p_{5yzz}p_{4yzz}p_{3yzz}p_{2yzz}p_{yzz} + \\
& p_{5zii}p_{4zii}p_{3zii}p_{2zii}p_{zii} + p_{5zix}p_{4zix}p_{3zix}p_{2zix}p_{zix} + \\
& p_{5ziy}p_{4ziy}p_{3ziy}p_{2ziy}p_{ziy} + p_{5ziz}p_{4ziz}p_{3ziz}p_{2ziz}p_{ziz} + \\
& p_{5zxi}p_{4zxi}p_{3zxi}p_{2zxi}p_{zxi} + p_{5zxx}p_{4zxx}p_{3zxx}p_{2zxx}p_{zxx} + \\
& p_{5zxy}p_{4zxy}p_{3zxy}p_{2zxy}p_{zxy} + p_{5zxz}p_{4zxz}p_{3zxz}p_{2zxz}p_{zxz} + \\
& p_{5zyi}p_{4zyi}p_{3zyi}p_{2zyi}p_{zyi} + p_{5zyx}p_{4zyx}p_{3zyx}p_{2zyx}p_{zyx} + \\
& p_{5zyy}p_{4zyy}p_{3zyy}p_{2zyy}p_{zyy} + p_{5zyz}p_{4zyz}p_{3zyz}p_{2zyz}p_{zyz} + \\
& p_{5zzi}p_{4zzi}p_{3zzi}p_{2zzi}p_{zzi} + p_{5zzx}p_{4zzx}p_{3zzx}p_{2zzx}p_{zzx} + \\
& p_{5zzy}p_{4zzy}p_{3zzy}p_{2zzy}p_{zzy} + p_{5zzz}p_{4zzz}p_{3zzz}p_{2zzz}p_{zzz} +
\end{aligned} \tag{A.26}$$

References

- [1] Rodney Van Meter and Simon J. Devitt. “The Path to Scalable Distributed Quantum Computing”. In: *Computer* 49.9 (2016), pp. 31–42. DOI: 10.1109/MC.2016.291.
- [2] Peter W. Shor. “Polynomial-Time Algorithms for Prime Factorization and Discrete Logarithms on a Quantum Computer”. In: *SIAM Journal on Computing* 26.5 (1997), pp. 1484–1509. DOI: 10.1137/s0097539795293172. URL: <https://doi.org/10.1137%2Fs0097539795293172>.
- [3] B. P. Lanyon et al. “Towards quantum chemistry on a quantum computer”. In: *Nature Chemistry* 2.2 (2010), pp. 106–111. DOI: 10.1038/nchem.483. URL: <https://doi.org/10.1038%2Fnchem.483>.
- [4] Aram W. Harrow, Avinatan Hassidim, and Seth Lloyd. “Quantum Algorithm for Linear Systems of Equations”. In: *Physical Review Letters* 103.15 (2009). DOI: 10.1103/physrevlett.103.150502. URL: <https://doi.org/10.1103%2Fphysrevlett.103.150502>.
- [5] P. Aliferis J. Preskill D. Gottesman. “Quantum accuracy threshold for concatenated distance-3 codes”. In: *Quant. Inf. Comput* 6 (2006), pp. 97–165. DOI: <https://dl.acm.org/doi/10.5555/2011665.2011666>.
- [6] A Yu Kitaev. “Quantum computations: algorithms and error correction”. In: *Russian Mathematical Surveys* 52.6 (1997), pp. 1191–1249. DOI: 10.1070/rm1997v052n06abeh002155. URL: <https://doi.org/10.1070/rm1997v052n06abeh002155>.
- [7] Laflamme Raymond Knill Emanuel and Zurek Wojciech H. “Resilient quantum computation: error models and thresholds”. In: *Proc. R. Soc. Lond. A* 454 (1998), pp. 365–384. DOI: <http://doi.org/10.1098/rspa.1998.0166>.
- [8] Daniel Gottesman. *An Introduction to Quantum Error Correction and Fault-Tolerant Quantum Computation*. 2009. DOI: 10.48550/ARXIV.0904.2557. URL: <https://arxiv.org/abs/0904.2557>.
- [9] Austin G. Fowler et al. “Surface codes: Towards practical large-scale quantum computation”. In: *Physical Review A* 86.3 (2012). DOI: 10.1103/physreva.86.032324. URL: <https://doi.org/10.1103%2Fphysreva.86.032324>.

- [10] S. B. Bravyi and A. Yu. Kitaev. *Quantum codes on a lattice with boundary*. 1998. DOI: 10.48550/ARXIV.QUANT-PH/9811052. URL: <https://arxiv.org/abs/quant-ph/9811052>.
- [11] Eric Dennis et al. “Topological quantum memory”. In: *Journal of Mathematical Physics* 43.9 (2002), pp. 4452–4505. DOI: 10.1063/1.1499754. URL: <https://doi.org/10.1063%2F1.1499754>.
- [12] Alexander Erhard et al. “Entangling logical qubits with lattice surgery”. In: *Nature* 589.7841 (2021), pp. 220–224. DOI: 10.1038/s41586-020-03079-6. URL: <https://doi.org/10.1038%2Fs41586-020-03079-6>.
- [13] Ashley M. Stephens. “Fault-tolerant thresholds for quantum error correction with the surface code”. In: *Phys. Rev. A* 89 (2 2014), p. 022321. DOI: 10.1103/PhysRevA.89.022321. URL: <https://link.aps.org/doi/10.1103/PhysRevA.89.022321>.
- [14] Craig Gidney et al. “A Fault-Tolerant Honeycomb Memory”. In: *Quantum* 5 (2021), p. 605. DOI: 10.22331/q-2021-12-20-605. URL: <https://doi.org/10.22331%2Fq-2021-12-20-605>.
- [15] Andrea Morello et al. “Donor Spins in Silicon for Quantum Technologies”. In: *Advanced Quantum Technologies* 3 (July 2020), p. 2000005. DOI: 10.1002/qute.202000005.
- [16] Mateusz T. Madzik et al. “Precision tomography of a three-qubit donor quantum processor in silicon”. In: *Nature* 601.7893 (2022), pp. 348–353. DOI: 10.1038/s41586-021-04292-7. URL: <https://doi.org/10.1038%2Fs41586-021-04292-7>.
- [17] Daniel Gottesman. *An Introduction to Quantum Error Correction and Fault-Tolerant Quantum Computation*. 2009. arXiv: 0904.2557 [quant-ph].
- [18] Simon J Devitt, William J Munro, and Kae Nemoto. “Quantum error correction for beginners”. In: *Reports on Progress in Physics* 76.7 (2013), p. 076001. DOI: 10.1088/0034-4885/76/7/076001. URL: <https://doi.org/10.1088%2F0034-4885%2F76%2F7%2F076001>.
- [19] Shota Nagayama et al. “Surface code error correction on a defective lattice”. In: *New Journal of Physics* 19.2 (2017), p. 023050. DOI: 10.1088/1367-2630/aa5918. URL: <https://doi.org/10.1088%5C%2F1367-2630%5C%2Faa5918>.

- [20] S. B. Bravyi and A. Yu. Kitaev. *Quantum codes on a lattice with boundary*. 1998. DOI: 10.48550/ARXIV.QUANT-PH/9811052. URL: <https://arxiv.org/abs/quant-ph/9811052>.
- [21] Michael H. Freedman and David A. Meyer. *Projective plane and planar quantum codes*. 1998. DOI: 10.48550/ARXIV.QUANT-PH/9810055. URL: <https://arxiv.org/abs/quant-ph/9810055>.
- [22] Andrew J. Landahl, Jonas T. Anderson, and Patrick R. Rice. *Fault-tolerant quantum computing with color codes*. 2011. DOI: 10.48550/ARXIV.1108.5738. URL: <https://arxiv.org/abs/1108.5738>.
- [23] Héctor Bombín. “Single-Shot Fault-Tolerant Quantum Error Correction”. In: *Physical Review X* 5.3 (2015). DOI: 10.1103/physrevx.5.031043. URL: <https://doi.org/10.1103%5C%2Fphysrevx.5.031043>.
- [24] Andrea Morello et al. “Single-shot readout of an electron spin in silicon”. In: *Nature* 467.7316 (2010), pp. 687–691. DOI: 10.1038/nature09392. URL: <https://doi.org/10.1038%2Fnature09392>.
- [25] M. A. Fogarty et al. “Integrated silicon qubit platform with single-spin addressability, exchange control and single-shot singlet-triplet readout”. In: *Nature Communications* 9.1 (2018). DOI: 10.1038/s41467-018-06039-x. URL: <https://doi.org/10.1038%5C%2Fs41467-018-06039-x>.
- [26] Panos Aliferis and John Preskill. “Fault-tolerant quantum computation against biased noise”. In: *Physical Review A* 78.5 (2008). DOI: 10.1103/physreva.78.052331. URL: <https://doi.org/10.1103%2Fphysreva.78.052331>.
- [27] P Aliferis et al. “Fault-tolerant computing with biased-noise superconducting qubits: a case study”. In: *New Journal of Physics* 11.1 (2009), p. 013061. DOI: 10.1088/1367-2630/11/1/013061.
- [28] Paul Webster, Stephen D. Bartlett, and David Poulin. “Reducing the overhead for quantum computation when noise is biased”. In: *Physical Review A* 92.6 (2015). DOI: 10.1103/physreva.92.062309.
- [29] Alan Robertson et al. “Tailored Codes for Small Quantum Memories”. In: *Physical Review Applied* 8.6 (2017). DOI: 10.1103/physrevapplied.8.064004.
- [30] Austin G. Fowler. “Coping with qubit leakage in topological codes”. In: *Physical Review A* 88.4 (2013). DOI: 10.1103/physreva.88.042308.

- [31] Joydip Ghosh et al. “Understanding the effects of leakage in superconducting quantum-error-detection circuits”. In: *Physical Review A* 88.6 (2013). DOI: 10.1103/physreva.88.062329. URL: <https://doi.org/10.1103%2Fphysreva.88.062329>.
- [32] J. I. Cirac and P. Zoller. “Quantum Computations with Cold Trapped Ions”. In: *Phys. Rev. Lett.* 74 (20 1995), pp. 4091–4094. DOI: 10.1103/PhysRevLett.74.4091. URL: <https://link.aps.org/doi/10.1103/PhysRevLett.74.4091>.
- [33] Mark S. Byrd et al. “Universal leakage elimination”. In: *Phys. Rev. A* 71 (5 2005), p. 052301. DOI: 10.1103/PhysRevA.71.052301. URL: <https://link.aps.org/doi/10.1103/PhysRevA.71.052301>.
- [34] B.E. Kane. “Silicon-based Quantum Computation”. In: *Fortschritte der Physik* 48.9-11 (2000), pp. 1023–1041. DOI: 10.1002/1521-3978(200009)48:9/11<1023::aid-prop1023>3.0.co;2-j.
- [35] Anasua Chatterjee et al. “Semiconductor qubits in practice”. In: *Nature Reviews Physics* 3.3 (2021), pp. 157–177. DOI: 10.1038/s42254-021-00283-9. URL: <https://doi.org/10.1038%5C%2Fs42254-021-00283-9>.
- [36] David K. Tuckett et al. “Tailoring Surface Codes for Highly Biased Noise”. In: *Phys. Rev. X* 9 (4 2019), p. 041031. DOI: 10.1103/PhysRevX.9.041031. URL: <https://link.aps.org/doi/10.1103/PhysRevX.9.041031>.
- [37] David K. Tuckett, Stephen D. Bartlett, and Steven T. Flammia. “Ultrahigh Error Threshold for Surface Codes with Biased Noise”. In: *Phys. Rev. Lett.* 120 (5 2018), p. 050505. DOI: 10.1103/PhysRevLett.120.050505. URL: <https://link.aps.org/doi/10.1103/PhysRevLett.120.050505>.
- [38] A.Yu. Kitaev. “Fault-tolerant quantum computation by anyons”. In: *Annals of Physics* 303.1 (2003), pp. 2–30. DOI: 10.1016/s0003-4916(02)00018-0. URL: <https://doi.org/10.1016%5C%2Fs0003-4916%2802%2900018-0>.
- [39] Alexei Kitaev. “Anyons in an exactly solved model and beyond”. In: *Annals of Physics* 321.1 (2006), pp. 2–111. DOI: 10.1016/j.aop.2005.10.005. URL: <https://doi.org/10.1016%5C%2Fj.aop.2005.10.005>.
- [40] Stephen D. Bartlett and Terry Rudolph. “Simple nearest-neighbor two-body Hamiltonian system for which the ground state is a universal resource for quantum computation”. In: *Physical Review A* 74.4 (2006). DOI: 10.1103/

- physreva.74.040302. URL: <https://doi.org/10.1103/5C%2Fphysreva.74.040302>.
- [41] Matthew B. Hastings and Jeongwan Haah. “Dynamically Generated Logical Qubits”. In: *Quantum* 5 (2021), p. 564. DOI: 10.22331/q-2021-10-19-564. URL: <https://doi.org/10.22331%5C%2Fq-2021-10-19-564>.
- [42] H. Bombin. “Topological subsystem codes”. In: *Phys. Rev. A* 81 (3 2010), p. 032301. DOI: 10.1103/PhysRevA.81.032301. URL: <https://link.aps.org/doi/10.1103/PhysRevA.81.032301>.
- [43] David S. Wang, Austin G. Fowler, and Lloyd C. L. Hollenberg. “Surface code quantum computing with error rates over 1%”. In: *Physical Review A* 83.2 (2011). DOI: 10.1103/physreva.83.020302.
- [44] H. Bombin. “Topological Order with a Twist: Ising Anyons from an Abelian Model”. In: *Physical Review Letters* 105.3 (2010). DOI: 10.1103/physrevlett.105.030403. URL: <https://doi.org/10.1103/5C%2Fphysrevlett.105.030403>.
- [45] Craig Gidney. *A Pair Measurement Surface Code on Pentagons*. 2022. DOI: 10.48550/ARXIV.2206.12780. URL: <https://arxiv.org/abs/2206.12780>.
- [46] Christopher J. Wood, Jacob D. Biamonte, and David G. Cory. “Tensor networks and graphical calculus for open quantum systems”. In: (2011). DOI: 10.48550/ARXIV.1111.6950. URL: <https://arxiv.org/abs/1111.6950>.
- [47] Daniel Greenbaum. *Introduction to Quantum Gate Set Tomography*. 2015. DOI: 10.48550/ARXIV.1509.02921. URL: <https://arxiv.org/abs/1509.02921>.
- [48] Jerry M. Chow et al. “Universal Quantum Gate Set Approaching Fault-Tolerant Thresholds with Superconducting Qubits”. In: *Physical Review Letters* 109.6 (2012). DOI: 10.1103/physrevlett.109.060501.
- [49] Alexander N. Korotkov. *Error matrices in quantum process tomography*. 2013. arXiv: 1309.6405 [quant-ph].
- [50] Erik Nielsen et al. “Gate Set Tomography”. In: *Quantum* 5 (2021), p. 557. DOI: 10.22331/q-2021-10-05-557. URL: <https://doi.org/10.22331%2Fq-2021-10-05-557>.

- [51] Zhenyu Cai and Simon C. Benjamin. “Constructing Smaller Pauli Twirling Sets for Arbitrary Error Channels”. In: *Scientific Reports* 9.1 (2019). DOI: 10.1038/s41598-019-46722-7. URL: <https://doi.org/10.1038/s41598-019-46722-7>.
- [52] Magesan, Easwar. “Gaining Information About a Quantum Channel Via Twirling”. 2008. URL: <http://hdl.handle.net/10012/3828>.
- [53] M. S. Anwar et al. “Practical implementations of twirl operations”. In: *Physical Review A* 71.3 (2005). DOI: 10.1103/physreva.71.032327. URL: <https://doi.org/10.1103/physreva.71.032327>.
- [54] Hou Shi-Yao et al. “Experimental Optimal Single Qubit Purification in an NMR Quantum Information Processor”. In: 4.1 (2014). DOI: <https://doi.org/10.1038/srep06857>.
- [55] Bikash K. Behera et al. “Demonstration of entanglement purification and swapping protocol to design quantum repeater in IBM quantum computer”. In: *Quantum Information Processing* 18.4 (2019). DOI: 10.1007/s11128-019-2229-2. URL: <https://doi.org/10.1007/s11128-019-2229-2>.
- [56] Yuval R Sanders, Joel J Wallman, and Barry C Sanders. “Bounding quantum gate error rate based on reported average fidelity”. In: *New Journal of Physics* 18.1 (2015), p. 012002. DOI: 10.1088/1367-2630/18/1/012002.
- [57] Qiskit contributors. *Qiskit: An Open-source Framework for Quantum Computing*. 2023. DOI: 10.5281/zenodo.2573505.
- [58] J.R. Johansson, P.D. Nation, and Franco Nori. “QuTiP: An open-source Python framework for the dynamics of open quantum systems”. In: *Computer Physics Communications* 183.8 (2012), pp. 1760–1772. ISSN: 0010-4655. DOI: <https://doi.org/10.1016/j.cpc.2012.02.021>. URL: <https://www.sciencedirect.com/science/article/pii/S0010465512000835>.
- [59] Gözde Üstün, Andrea Morello, and Simon Devitt. *Error Analysis in the context of Quantum Error Correction*. Version 1.0.0. Apr. 2023. URL: <https://github.com/apassenger/Error-Analysis-in-QEC>.
- [60] Gerald Waldherr et al. “Quantum error correction in a solid-state hybrid spin register”. In: *Nature* 506.7487 (2014), pp. 204–207. DOI: 10.1038/nature12919.

- [61] Bas Hensen et al. “A silicon quantum-dot-coupled nuclear spin qubit”. In: *Nature Nanotechnology* 15.1 (2020), pp. 13–17. DOI: doi.org/10.1038/s41565-019-0587-7.
- [62] Andrea Morello et al. “Donor spins in silicon for quantum technologies”. In: *Advanced Quantum Technologies* 3.11 (2020), p. 2000005. DOI: doi.org/10.1002/qute.202000005. URL: <https://onlinelibrary.wiley.com/doi/full/10.1002/qute.202000005>.
- [63] Khaneja N et al. “Optimal control of coupled spin dynamics: design of NMR pulse sequences by gradient ascent algorithms”. In: *Journal of Magnetic Resonance* 172.2 (2005), pp. 296–305. ISSN: 1090-7807. DOI: <https://doi.org/10.1016/j.jmr.2004.11.004>. URL: <https://www.sciencedirect.com/science/article/pii/S1090780704003696>.
- [64] Boxi Li et al. “Pulse-level noisy quantum circuits with QuTiP”. In: *Quantum* 6 (2022), p. 630. DOI: [10.22331/q-2022-01-24-630](https://doi.org/10.22331/q-2022-01-24-630).
- [65] C. A. Ryan et al. “Liquid-state nuclear magnetic resonance as a testbed for developing quantum control methods”. In: *Physical Review A* 78.1 (2008). DOI: [10.1103/physreva.78.012328](https://doi.org/10.1103/physreva.78.012328).
- [66] Christiane P. Koch et al. “Quantum optimal control in quantum technologies. Strategic report on current status, visions and goals for research in Europe”. In: *EPJ Quantum Technology* 9.1 (2022). DOI: [10.1140/epjqt/s40507-022-00138-x](https://doi.org/10.1140/epjqt/s40507-022-00138-x).
- [67] D. G. Cory et al. “Experimental Quantum Error Correction”. In: *Phys. Rev. Lett.* 81 (10 1998), pp. 2152–2155. DOI: [10.1103/PhysRevLett.81.2152](https://doi.org/10.1103/PhysRevLett.81.2152). URL: <https://link.aps.org/doi/10.1103/PhysRevLett.81.2152>.
- [68] Jingfu Zhang et al. “Experimental quantum error correction with high fidelity”. In: *Physical Review A* 84.3 (2011). DOI: [10.1103/physreva.84.034303](https://doi.org/10.1103/physreva.84.034303).
- [69] Richard H. Byrd et al. “A Limited Memory Algorithm for Bound Constrained Optimization”. In: *SIAM Journal on Scientific Computing* 16.5 (1995), pp. 1190–1208. DOI: [10.1137/0916069](https://doi.org/10.1137/0916069).
- [70] Richard H. Byrd et al. “A Limited Memory Algorithm for Bound Constrained Optimization”. In: *SIAM Journal on Scientific Computing* 16.5 (1995), pp. 1190–1208. DOI: [10.1137/0916069](https://doi.org/10.1137/0916069). eprint: <https://doi.org/10.1137/0916069>.

- [71] Gözde Üstün et al. *Implementing-XX-Single-Step-Parity-Check-Gate-on-Silicon-Spin-System*. Version 1.0.0. Apr. 2023. URL: <https://github.com/apassenger/Implementing-XX-Single-Step-Parity-Check-Gate-on-Silicon-Spin-System>.
- [72] Gözde Üstün et al. *CNOT Gate Implementation on Silicon Spin System Using GRAPE Algorithm*. Version 1.0.0. Apr. 2023. URL: https://github.com/apassenger/CNOT_gate_implementation_with_Grape.
- [73] Rostyslav Savytsky et al. *An electrically-driven single-atom ‘flip-flop’ qubit*. 2022. DOI: 10.48550/ARXIV.2202.04438. URL: <https://arxiv.org/abs/2202.04438>.